Antimony selenide based solar cells

Fabrication, characterisation, and modelling towards development of bifacial solar cells

Tobias Verheugen Hvidsten

Master Thesis

Renewable Energy Systems

60 credits

Department of Technology Systems

The Faculty of Mathematics and Natural Sciences

UNIVERSITY OF OSLO

May / 2022

Antimony selenide based solar cells

Fabrication, characterisation, and modelling towards development of bifacial solar cells

Tobias Verheugen Hvidsten

2022

Antimony selenide based solar cells

Tobias Verheugen Hvidsten

http://www.duo.uio.no/

Printed: Reprosentralen, Universitetet i Oslo

Abstract

This thesis investigates the promising solar cell absorber layer antimony selenide with the goal to work towards the use of the material in bifacial solar cells. Antimony selenide is a material which is abundant on earth and which shows properties making is very suitable for the as the absorber layer of solar cells.

Antimony selenide based solar cells was investigated both experimentally and through modelling. For the experiments both monofacial samples incorporation P3HT, an organic hole transport layer, and bifacial samples utilising the transparent conducting oxide ITO was fabricated. The samples were characterised from both sides of the samples, using current – voltage and external quantum efficiency measurements. The solar cells were modelled in order to further investigate properties of the solar cells, and to show what efficiencies could potentially be obtained from antimony selenide based solar cells.

The results of the thesis show a promising first step towards the development of bifacial antimony selenide based solar cells. Through the addition of the P3HT hole transport layer in the monofacial solar cell, the material was shown to beneficial for the current of the solar cell. It was further shown by modelling that the incorporation of hole transport layer was advantageous to the efficiency of the bifacial solar cells. The fabricated bifacial solar cells with ITO back contact showed large losses compared to the monofacial samples with gold as the back contact. Through modelling it was shown that the losses could potentially be caused by ITO forming a rectifying contact on the back side of the solar cell, preventing the collection of the photogenerated carriers. Further the modelling showed high efficiencies for the bifacial solar cells by increasing the work function of ITO.

Acknowledgments

I would like to thank my supervisors for great guidance and feedback throughout my work with this thesis. Main supervisor Smagul Karazhanov and co-supervisors Nicolae Spalatu and Sabrina Sartori. Thank you for letting me take part in your exciting research.

Also a special thank to Nicolae Spalatu and the rest of the research group at the Laboratory of Thin Film Chemical Technologies at Tallinn University of Technology for the warm welcome during my exchange to Estonia.

Contents

List of figures

List of tables

List of abbreviations and nomenclature

Abbreviations

FF Fill Factor

PCE Power Conversion Efficiency

HTL Hole Transport Layer

TCO Transparent Conductive Oxide

ITO Indium Tin Oxide

FTO Fluorine doped Tin Oxide

MPP Maximum Power Point

EQE External Quantum Efficiency

CSS Close Space Sublimation

USP Ultrasonic spray pyrolysis

STC Standard Test Conditions

Nomenclature

J_{sc} Short circuit current density,

V_{oc} Open circuit voltage,

1 Introduction

Global warming and climate change is a major challenge for the world today. It is widely accepted that the cause of the global warming is emissions of greenhouse gases, mainly carbon dioxide. In order to mitigate the consequences of changes in the climate, it is necessary to limit global warming by reducing the emissions of greenhouse gases. A major source of greenhouse gas emissions comes from the burning of fossil fuels such as oil, coal and gas. For the total electricity production in the world in 2019, fossil fuels such as coal (36.7 %), oil (2.8 %) and natural gas (23.5 %) made up a total of 63 % (IEA, 2021). Renewable energy sources such as hydro (16 %), wind (5.4 %) and solar (2.6 %) made up a total of 24 %. Through the transition away from fossil fuel-based energy generation towards renewable sources of energy the greenhouse gas emissions from the energy sector can be reduced, and through that contribute to mitigate the consequences of global warming and climate change. One such renewable source of energy with immense potential is solar energy. Solar energy is the driving force behind other renewable energy sources such as wind and hydro, but through photovoltaics (PV) irradiation from the sun can be directly transformed into electricity.

Despite solar energy only standing for 2.6 % of the total electricity generation in the world in 2019 (IEA, 2021), it is expected that solar PV will become a major source of electricity in the future. For 2020 it is reported an installed capacity of solar PV of 145 GW (IEA-PVPS, 2021, p. 10). With an installed capacity in the world at the end of 2019 of 622 GW, the installed capacity in 2020 accounted for an increase of over 23 %. In addition, of the 767 GW total installed PV capacity at the end of 2020, according to IEA PVPS 70 % of this was installed only during the previous five years, that is between the start of 2016 and end of 2020.

Solar PV has experienced an immense growth, and despite only accounting for a very small part of the market this might change as the growth is not expected to stop. DNV has forecasted that of the total grid connected electricity generation in 2050, solar PV will make up 36 % of it (DNV, 2021, p. 87). Based on this it is safe to say that solar PV is an important source of renewable energy, and which increasingly becomes more important, and thus also makes an important contribution in the reduction of greenhouse gas emissions. This of course motivates the research on the topic, to further improve solar PV technology.

The PV market is today dominated by crystalline silicon based solar cells, with thin film solar cells only constituting a few percentages of the total market. 2020 production of PV was reported to consist of 143.9 GWp crystalline silicon (monocrystalline and multicrystalline together) and 7.7 GWp thin film PV (Philipps & Warmuth, 2022). Resulting in a market share of 94.9% for crystalline silicon, with thin film technologies making up the remaining 5.1%. Both crystalline silicon based solar cells and the thin film technologies in the market have achieved high efficiencies. State of the art efficiencies of crystalline silicon is 26.7%, correspondingly we have 23.35% and 21.0% for CIGS and CdTe respectively (Green et al., 2022). For modules record efficiencies are lower for all technologies. 24.4% for crystalline silicon, 19.2% for CIGS and 19.0% for CdTe.

In addition to the distinction between solar cells based on absorber material, solar cells can also be divided into monofacial and bifacial solar cells. Simply said the difference between a monofacial and bifacial solar cell is that monofacial cells can only utilise solar irradiation incident on the front side, while bifacial cells are transparent on both sides. This means that bifacial solar cells can utilise irradiation incident on both sides. The advantage of the bifacial PV is that it can capture more light for a given area, and according to IEA PVPS the use of bifacial PV with single axis tracking can obtain gains in energy production up to 35 % (IEA-PVPS, 2021, p. 8). While monofacial historically have dominated the market, bifacial PV is becoming more common and it is forecasted that it will have a market share of 60 % by 2032 (VDMA, 2022, p. 45)

Solar cell technologies are commonly classified into three generations. In the first generation we find crystalline silicon based solar cells. In the second generation we find thin-film technologies such as CdTe and CIGS. Finally, in the third generation we find thin-film solar cells based on novel absorber materials (MIT, 2015, p. 31). This work considers antimony selenide based solar cells, a third-generation technology.

1.1 Motivation

Antimony selenide is a semiconductor showing great potential for PV applications. But there already is well developed and mature PV technology in the market, so before we go into details

on antimony selenide, we must ask the following question: Why is there a need of developing antimony selenide based solar cells instead of using already developed technologies? To answer this question, we must take a look at the technologies currently dominating the PV market.

The first generation of solar cells were silicon based solar cells. Silicon based solar modules holds the highest market share today and also exhibits the highest efficiencies. These first-generation solar cells are based on silicon wafers, so there is no need for a substrate such as glass (MIT, 2015, pp. 22-24). However, this is where the main issue occurs. The absorption of light in crystalline silicon based solar cells is low. In order to absorb enough light to obtain efficient solar cells, thick wafers in the order of 100 μm is necessary. Because of this thick wafer there is a high material usage.

The second generation of solar cells solves the problem with the thick absorber of the crystalline silicon first generation solar cells. In contrast to the first generation, the second generation is not wafer based (MIT, 2015, pp. 22, 26). Instead, the solar cell is made by the use of a substrate such as glass on which the different layers of the thin film solar cell is deposited. CIGS and CdTe are examples of such thin film solar cells which exists in the market today. These technologies utilise absorber materials which absorb light much easier than crystalline silicon. The result of this is that for the absorber materials used, a much thinner layer is needed in order to absorb the same wavelengths of light as the silicon based first generation solar cells. The film thickness needed is only in the order of a few micrometres. It is clear that this thickness which is only a fraction of that of silicon also results in a much lover material usage. These thin film technologies do, however, only have a market share of about 5% (Philipps & Warmuth, 2022). One reason for this might be the lower power conversion efficiencies of the thin film solar cells compared to the crystalline silicon ones. There is, however, another important aspect of CIGS and CdTe thin film solar cell that might limit the growth of these technologies. Because both CIGS and CdTe utilises materials which are either non-abundant or toxic. In CdTe the toxic material cadmium (Cd) is used, while the non-abundant materials tellurium and indium is used in CdTe and CIGS respectively. Especially the use of non-abundant materials might become limiting despite the low material usage.

The goal with further development is then to find earth abundant and non-toxic materials to use in solar cells, while keeping the advantages with the high absorption coefficient enabling thin

film solar cells from the second generation. The question to ask is then “What material can be used to solve the issues with previous generation solar cells?” This is where antimony selenide comes into the picture. Antimony selenide is an abundant, non-toxic material with a high absorption coefficient (Mavlonov et al., 2020). With these properties antimony selenide appears as a promising candidate to achieve cheaper and more sustainable thin film solar cells. Of course, antimony selenide is not without its challenges. Currently the efficiency of antimony selenide based solar cells is far from what is needed in order for the technology to be commercial, with the current state of the art efficiency standing at 9.2% as reported in 2019 (Li et al., 2019). There is a need to improve this efficiency, and what this thesis aims to do is make a contribution to the development of antimony selenide based solar cells. The following section defines three research questions, which summarise the work which will be conducted in this thesis to address some of the current issues for antimony selenide based solar cells.

1.2 Research questions

The thesis is investigating antimony selenide both experimentally and through modelling. The work can be summarised in the three following research questions

1. Can using a P3HT hole transport layer improve the efficiency of the antimony selenide based solar cell?
2. What is the effect of using a transparent back contact (ITO) on the performance of the antimony selenide based solar cell under front and rear side illumination?
3. What thickness and doping level of the antimony selenide absorber results in the best performance of the antimony selenide based solar cell?

The first research question considers hole transport layers. Hole transport layers are materials used to prevent recombination on the back side of the solar cell and increase the collection of carriers (Li et al., 2018). The P3HT material has been applied as hole transport layer and proved to be effective for perovskite solar cells (Li et al., 2021). This motivates the attempt to apply the same material for the antimony selenide based solar cells. As mentioned, the efficiency of antimony selenide based solar cells is still lacking, and this step was taken in order to improve the performance of the solar cell.

The second research question is asking if the antimony selenide based solar cells can be made bifacial, and specifically if the transparent conductive oxide ITO can be applied as a replacement to the non-transparent gold back contact of the monofacial cells, and as such achieve bifaciality. By bifacial it is meant that the backside of the solar cell is made transparent so that light can enter the solar cell from both sides. This means that more light can enter and be collected by the solar cell, resulting in a higher current and thus higher power from a given area. The choice of applying ITO as the back contact is motivated by its performance in other works, where it has been shown to be suitable as a back contact (Schneider et al., 2022). While antimony selenide still is under active research and far from being a technology that is ready to be commercially available, it is still interesting to investigate the opportunity to utilise the material for other solar cell technologies such as bifacial solar cells. This is motivated by the forecasted increased use of bifacial solar PV. Combining antimony selenide solar cells and the bifacial solar cell concept gives a promising concept of more sustainable and better performing solar cells, producing more electricity for a given area.

These two first research questions were solved experimentally by introducing the layers into the antimony selenide based solar cells and were then characterised to assess the effect this had on the performance. In contrast the third research question will be solved through modelling. Experimental results for antimony selenide based solar cells show low power conversion efficiencies compared to the power conversion efficiencies achieved by the thin film second generation solar cells. It is important to motivate the use of a material by illustrating its potential. As this cannot be done through experiments, modelling will be used to investigate the potential of antimony selenide based solar cells. The focus is mainly on analysing the effect of changing the thickness and doping of the absorber. Optimisation of the thickness of the absorber is the balance of the absorption of light and recombination, as both increase for thicker films. The effect the free carrier concentration has on efficiency is investigated by changing the doping. One major issue is that it is yet not known how to experimentally control the electrical conductivity, through doping, of antimony selenide. This can, however, be done with modelling. Investigating the doping is important to show the potential of the technology when control of doping is achieved also experimentally.

2 Theory and literature

This chapter will describe the solar cells considered in this work and the theory behind both the solar cells and the methods applied for characterisation and modelling.

2.1 Solar cells (PV, photovoltaic effect, p-n junction)

Solar cells are devices which can directly convert solar irradiation into electricity.

2.1.1 Semiconductors

Fundamental to solar cells is the semiconductor. A semiconductor is a material with properties in between metals and insulators (Streetman & Banerjee, 2016, pp. 87-88). This type of material is characterised by its band gap, a range of energies which no electrons can occupy. Below the bandgap is the valence band and above the bandgap is the conduction band. At low temperatures and with no illumination electrons are situated in the valence band, and in this case acts as an insulator because there are no empty states in the valence band in which the electrons can move. However, in semiconductors electrons can be thermally or optically excited across the band gap and to the conduction band if the energy supplied are at least the energy of the band gap. With electrons excited across the band gap to the conduction band they are free to move about the many empty states there. In addition, the excited electron leaves behind a hole in the valence band, which is free to switch places with the electrons. Through this the semiconductor becomes conductive. Semiconductors does, however, have the property that when illuminated by photons with energies higher than the band gap, electrons can be excited across the band gap from the valence band to the conduction band. When an electron is exited to the conduction band it is free to move between the many empty states there. The excited electron also leaves behind an empty state in the valence band, which is free to move around between all the electrons there.

2.1.2 P-n junction

Solar cells utilise the semiconductors property of light generated electron hole pairs. However, in order to obtain a current and voltage from these light generated electron hole pairs, they must be separated to prevent them from recombining. This is where the p-n junction comes into the picture. A p-n junction is two semiconductors put together, where one of these semiconductors

are p-type while the other is n-type (Honsberg & Bowden, 2019). Semiconductors can be intrinsic, p-type or n-type. Intrinsic semiconductors have equal amounts of electrons in the conduction band as holes in the valence band, while n- and p-type semiconductors exhibit excess concentrations of electrons and holes respectively. Doping is the common method used to obtain n- or p-type semiconductors. This is achieved by introducing atoms in the semiconductor which either can donate an electron to the conduction band or is lacking an electron so that a hole occurs in the valence band. Doping is used to increase the conductivity of the semiconductor by creating more free carriers. At this p-n junction electrons diffuse to the p-side and holes to the n-side. Ions are left behind (positive in the n-type and negative in the p-type) causing an electric field to arise. The electric field is directed so that electrons drift from the p-type to the n-type, while holes drift from the n-type to the p-type. When a photogenerated electron hole pair is created, the minority carrier (the minority carrier is holes in n-type and electrons in p-type) drift across the junction and become majority carriers due to the electric field. To recombine the carriers have to travel through the external circuit, thus creating a current. A voltage is created when the separated electron hole pairs is prevented from entering the external circuit, causing a build-up of charge on either side of the p-n junction.

2.2 Antimony selenide based solar cells

As mentioned in the introduction, antimony selenide is a promising material for photovoltaic applications. Antimony selenide has been found to be suitable for application as the light absorbing layer in thin film solar cells. This is due to its favourable properties such as suitable bandgap and high absorption coefficient (high absorption of light), in addition to the advantages of it being a non-toxic and earth abundant material (Mavlonov et al., 2020). An indirect band gap of 1.03 eV and direct band gap of 1.17 eV are reported for antimony selenide (Chen et al., 2015). Antimony selenide (Sb_2Se_3) is a compound semiconductor consisting of the two elements antimony (Sb) and selenium (Se). Solar cells based on antimony selenide have shown promise with the reported experimental power conversion efficiency having increased dramatically from around 2% reported only in 2014 (Mavlonov et al., 2020) to the current state of the art cell having reached a record efficiency of 9.2% in 2019 (Li et al., 2019). This large increase in reported PCE achieved in only a few years is very promising, but antimony selenide based solar cells are still far from reaching the efficiencies of more mature thin film technologies such as CIGS and CdTe, with reported record laboratory efficiencies of 23.4% and 21.0% respectively.

Antimony selenide exhibits a one-dimensional crystal structure, resulting in properties depending on the orientation of the crystal. It has been found that carrier transport is higher along the one-dimensional crystal ribbons than across them, and that it, therefore, is beneficial for the one-dimensional ribbons to be orientated perpendicularly on the substrate (Li et al., 2019; Mavlonov et al., 2020). Undoped antimony selenide is used for the absorber. The doping concentration in the order of 10^{16} cm^{-3} is optimal for the absorber, but the reported free carrier concentration is much lower at 1.8×10^{13} cm^{-3} (Chen et al., 2017).

2.2.1 The layers of the solar cell

The structure with the different layers of the antimony selenide based solar cells considered in this thesis is shown Figure 1. The solar cells have a superstrate structure, meaning that when the solar cells are fabricated one starts with the front side of the solar cells (Mavlonov et al., 2020). The frontside meaning the side facing the sun. Glass is used as the substrate for the deposition of the subsequent layers, which is applied in the order shown in the figure. Starting with the transparent electrode, or the front contact, the material used for this layer is fluorine doped tin oxide (FTO). FTO is a transparent conductive oxide (TCO) which have the property of being both conductive and transparent. The buffer used is titanium dioxide (TiO_2) and the absorber is antimony selenide (Sb_2Se_3). The basic functionality of a solar cell as described in the previous section is also how the antimony selenide based solar cells work. The TiO_2 buffer and the Sb_2Se_3 absorber together makes up the p-n junction, with the buffer being the n-type semiconductor of the junction and the absorber being the p-type semiconductor.

The absorber is the main layer of the solar cell, the one made of antimony selenide, and makes up the p-side of the p-n junction. It is in this layer that the photons are absorbed and converted into electron-hole pairs. The antimony selenide absorber for the current record efficiency holder for antimony selenide based solar cells of 9.2% was deposited using close space sublimation (CSS) (Li et al., 2019). This deposition method is also applied for the absorber in this work. A two-step deposition method is applied where first a seed layer is created before the main layer of the absorber was grown on this seed layer. This deposition method has been shown to provide substantial increases in efficiency (Hutter et al., 2018; Krautmann et al., 2021). This two-step method with a seed layer have been shown to improve the performance of the solar cell

compared to a similar solar cell without the seed layer, with the efficiency shown to increase from 1.6% to 3.8% (Krautmann et al., 2021).

The photogenerated electrons in the absorber is collected by the buffer because of the electric field in the p-n junction between the buffer and the absorber. Because the photogeneration is to happen in the absorber, the semiconductor of the buffer should have a high bandgap to avoid light being absorbed here instead of in the absorber (Mavlonov et al., 2020). For photons with energies higher than the buffer band gap, these can be absorbed in the buffer instead of the absorber, resulting in a loss. The buffer used for all the samples in this thesis is TiO_2, which is a n-type material. CdS is a material more commonly applied as the buffer layer in thin film solar cells, also for antimony selenide based solar cells. However, this material has drawbacks such as toxicity, lattice mismatch (can cause degradation of performance) and low bandgap (meaning that light will be absorbed in the buffer instead of the absorber). For these reasons other buffer layers are investigated, such as TiO_2 (Mavlonov et al., 2020).

So far the two main layers of the solar cell, the buffer and absorber have been discussed. The experimental part of this work, however, focuses on the hole transport layer and back contact. The samples in the thesis can be divided into three main categories. These three categories are monofacial reference samples, monofacial samples with hole transport layer and bifacial samples. Common for all the samples in each of these categories is that they all have the same glass substrate, FTO front contact, TiO_2 buffer and Sb_2Se_3 absorber. It is in the layers after the absorber that the differences between the different categories occur. The only differences are found in the inclusion of a hole transport layer between the absorber and BC and replacement of the gold back contact with ITO for the bifacial samples. The reference samples have the structure as described above and then with the back contact of gold deposited directly on the absorber. The sample with hole transport layer is identical to the reference only with the inclusion of the P3HT hole transport layer in between the absorber and the back contact. The bifacial cells are the same as the reference, meaning without hole transport layer, but with a transparent back contact. The transparent back contact is either pure ITO or ITO with a thin layer of gold in between the absorber and the ITO. The gold layer between the absorber and the ITO back contact is so thin that it should be transparent, but still contribute to improving the interface between the ITO and absorber.

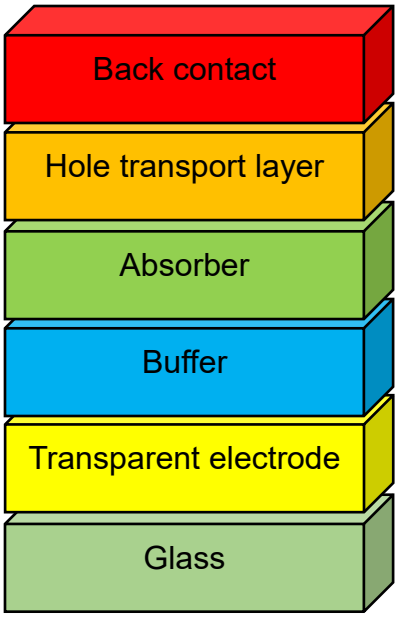

Figure 1: The structure of the solar cells.

2.2.2 Hole transport layer

A hole transport layer (HTL) is a material introduced between the absorber and back contact of the solar cell. The HTL investigated here is P3HT, short for poly(3-hexylthiophene), which is an organic semiconductor (Li et al., 2018). The hole transport layer is introduced in order to create a back surface field at the junction between the absorber and HTL, which should improve the collection of holes and reduce the recombination on the back contact of the solar cell.

The back surface field is created because the HTL has a higher concentration of holes, it is more p-type, than the absorber (Honsberg & Bowden, 2019). This junction works similarly to a p-n junction. Holes are collected by the HTL while it prevents electrons from reaching and recombining at the back contact. An improved collection of holes and a reduced recombination means that the power conversion efficiency of the solar cell is improved.

2.2.3 Bifacial solar cells

Bifacial solar cells do not only allow light to be collected from the front surface of the solar panels, but also from the backside. In this way light incident on the backside can contribute to carrier generation. The difference between a monofacial and bifacial solar cell can be minor. For a solar cell structure consisting only of a p-n junction with a contact on either side, the idea is simple. Since it is in the p-n junction the light is captured and turned into electron-hole pairs, we understand that the contacts must be transparent for this to happen. For monofacial cell the

front contact is usually a transparent conductive oxide (TCO), a type of material which is transparent as well as having a high conductivity (Mavlonov et al., 2020). The back contact, however, is not transparent, commonly made of a metal, such as gold. The bifacial solar cell differs from this in that it is using a transparent contact on both the front side and back side of the solar cell, allowing light to enter from both sides. A transparent conductive oxide shown to be suitable for application as the back contact for solar cells is ITO, despite it being a n-type material (Schneider et al., 2022).

Bifacial solar cells based on antimony selenide have not been reported in the literature. Bifacial solar cells based on other thin film technologies have, however. For instance, bifacial solar cells based on one of the biggest thin film solar cell technologies in the market today, CdTe, have been reported. CdTe based bifacial solar cells utilising ITO as back contact have reported efficiencies of 11.6 % under front side illumination and 5.5 % under back side illumination (Pokhrel et al., 2022) . However, this sample used a hole transport layer, and the efficiencies when using ITO without the HTL was reported as 7.0 % and 1.1 % for the front and back side respectively.

As seen from the efficiencies of CdTe based bifacial devices given above, there is a clear difference between the efficiency of the front and back side of the solar cell. This is explained by carriers being less efficiently collected under back side illumination due to the distance from the p-n junction the carriers are generated (Pokhrel et al., 2022). Under front side illumination the light passes through the transparent electrode and buffer layer before it reaches the absorber where most of the electron hole pairs are generated close to junction, and the electrons are then easily collected by the buffer. When the cell is illuminated from the back side, on the other hand, the photons are absorbed close to the back contact, on the side of the absorber furthest away from the p-n junction. This causes more electron-hole pairs to be generated further away from the junction than for front side illumination. This is far from the electric field separating the electron hole pair, and so there is an increased chance of recombination because of the longer distance the electrons have to travel through the absorber before being collected by the buffer.

2.3 Material and solar cell characterisation

Five different methods for characterisation are used for the characterisation of the solar cells and individual materials from the solar cells in this thesis. Three of these methods, UV-Vis, XRD and hot probe, are used to determine characteristics of the individual materials of the solar cell. For the remaining two methods, current density-voltage (J-V) curve and external quantum efficiency (EQE), which are two of the most important measurement for characterisation of solar cells, are used for solar cell characterisation with the goal of assessing the performance of the solar cells. In the following five subsection each of these mentioned characterisation methods will be explained and detailed.

2.3.1 Ultraviolet-visible spectroscopy

UV-Vis, short for ultraviolet-visible spectroscopy, is used to measure transmittance and reflectance. The reason for why we want to measure transmittance and reflectance in this work is that we can use it to calculate the absorption coefficient and from it the band gap of the semiconductor material can be extracted. From transmittance and reflectance measured with UV-Vis, the absorption coefficient can be calculated, which in turn can be used to estimate the band gap of the material measured. Calculation of the absorption coefficient from the transmittance and reflectance is given by the formula

$$\alpha = -\frac{1}{d} ln\left(\frac{T}{1-R}\right) = \frac{1}{d} ln\left(\frac{1-R}{T}\right) \quad (1)$$

where d is the thickness of semiconductor film the measurements are performed on, R is the reflectance and T is the transmittance (Carron et al., 2019; Černošková et al., 2014).

Having the absorption coefficient, the band gap of the semiconductor can be calculated using the relation

$$(\alpha h\nu)^{\gamma} = A\left(h\nu - E_g\right) \quad (2)$$

where A is a constant, $h\nu$ is the energy of a photon and E_g is the band gap. The value of the exponent γ depends on whether we are dealing with a semiconductor with a direct or indirect band gap. For a direct band gap we have $\gamma = 2$, while we have $\gamma = 1/2$ for indirect band gaps (Chen et al., 2015). The reported indirect band gap of 1.03 eV and direct band gap of 1.17 eV

for antimony selenide (Chen et al., 2015) and the reported 1.9 eV band gap of P3HT (Dadhich et al., 2021) were both obtained using this method.

2.3.2 X-Ray Diffraction

X-ray diffraction (XRD) is used to investigate the orientation of the crystal structure in the antimony selenide absorber. Considering the crystal structure to make up planes on which x-rays are reflected. The basic theory is given by the Bragg condition (Streetman & Banerjee, 2016)

$$n\lambda = 2d \sin\theta \tag{3}$$

which says that if the difference in distance x-rays reflected from parallel planes have to travel is equal to λ, the wavelength of the x-ray, multiplied by an integer n, then constructive interference occurs. This difference in distance is given by the right-hand side of equation **Error! Reference source not found.**, where d is the distance between the parallel planes and is the angel between the plane and the x-ray. (Hofmann, 2015, pp. 7-8) A peak in the XRD measurements thus indicated that the Bragg condition is met, and constructive interference occurs for the x-ray reflected from the parallel the crystal planes.

As previously mentioned, antimony selenide exhibits properties dependent on the orientation of the crystal. Meaning that certain orientations of the crystal is advantageous over other, so XRD is used to investigate whether or not optimal orientation is achieved. For antimony selenide it was reported strong peaks for the (211) crystal orientation at 28.4° and (221) crystal orientation at 31.4°, while there is a lack of a considerable peak for the (120) crystal orientation at 17° indicates a preferred orientation of the crystals in the absorber (Hutter et al., 2018).

2.3.3 Hot Probe

Hot probe measurement is a method to measure the conductivity type of semiconductor. Semiconductors can either be p-type, where there is an excess of holes compared to electrons, or n-type, which means that there is an excess of electrons compared to holes. Normally n-type or p-type conductivity is achieved by doping. Doping with a donor gives an extra electron to the conduction band of the material causing n-type conductivity, while doping with an acceptor causes an electron to be trapped, leaving behind a hole in the valence band and thus causing p-

type conductivity. However, some intrinsic semiconductors, that is undoped, shows p- or n-type conductivity, which is the case with antimony selenide and the reason for doing this measurement.

The principle of the method is as follows. Two probes are placed on the semiconductor film, one of which, is heated. What happens when the probe is heated is that the free carriers close to the probe are supplied with energy. Because of this the carriers will start to diffuse away from the probe in order to distribute the energy evenly in the film. Because of this diffusion of charge carriers away from the heated probe a voltage is built up between the probes. There are two possible outcomes of these measurements, depending on whether the material being measured is n-type or p-type. For a p-type material the free charge carriers are holes. When the hot probe increases the energy of the nearby holes, they diffuse away, leaving behind negative charges. The positive charged holes move to other parts of the material causing net positive charge in these areas. The negative charges cause the voltage to be lower at the heated probe than at the non-heated probe, giving a negative voltage. For the opposite case, with n-type material, the free charge carriers are not holes but electrons. It is the electrons that are provided with energy from the heated probe and diffuses away, leaving behind positively charged holes. While the negatively charged electrons cause negative charge in other parts of the film. This positive charge at the hot probe results in a positive voltage measured between the films.

2.3.4 J-V

The performance of the solar cell can be expressed through the J-V curve (Pearsall, 2017). What the J-V curve gives is the current density (J) as a function of voltage (V). The measurements to obtain the J-V (current density-voltage) curve of the solar cell are performed in a solar simulator. What is actually measured in the solar simulator is the I-V curve, current and voltage, but the current is turned into the current density simply by dividing by the area of the solar cell. The solar simulator is operating under standard test conditions. The standard test conditions (STC) are used because the performance of a solar cell varies depending on the conditions it is operating in. Consequently, the standard test conditions give the conditions to test solar cells under, which ensures that performance can be compared between different measurements and technologies. The standard test conditions are defined as follows 1000 W/m^2 irradiance, AM1.5

standard global spectrum, 25°C operating temperature and normal incidence irradiance (Pearsall, 2017).

Important performance indicators such as fill factor (FF) and power conversion efficiency (PCE) can be extracted from the J-V curves. These are the fundamental measures of the performance of the solar cell. Directly from the J-V curve can short circuit current density and open circuit voltage be extracted. Short circuit current density (J_{sc}) gives the maximum current of the solar cell and is found from the J-V curve where there is no voltage. The open circuit voltage (V_{oc}) gives the maximum voltage and is found from the J-V curve where the solar cell gives no current. The power (P) of the solar cell is calculated by multiplying the current density by the voltage

$$P = J \cdot V \tag{4}$$

Following this we get the power-voltage curve, giving the power as a function of voltage. The maximum power point (MPP) is defined as the point where the highest power from the solar cell is obtained. This is the point we want the solar cell to operate on as it here it delivers power to its full potential. At the maximum power point we find the maximum power from the solar cell (P_{max}). Voltage at maximum power point (V_{mpp}) and current density at maximum power point (J_{mpp}) is simply the voltage and current density giving the maximum power. Knowing the maximum power point characteristics, the open circuit voltage and the short circuit current the fill factor (FF) can be calculated. It is defined as

$$FF = \frac{J_{mpp} \cdot V_{mpp}}{J_{sc} \cdot V_{oc}} = \frac{P_{max}}{J_{sc} \cdot V_{oc}} \tag{5}$$

The fill factor is usually given as a percentage. The fill factor is the area under the maximum power point of the J-V curve divided by the area of square spanned by the short circuit current density and the open circuit voltage. The square spanned by the short circuit current density and open circuit voltage represents the ideal shape of the J-V curve without any losses. Consequently, the fill factor gives how much of this ideal area is spanned by the measured J-V curve. Finally, the power conversion efficiency (PCE) is defined as

$$PCE = \frac{J_{mpp} \cdot V_{mpp}}{G_i} = \frac{P_{max}}{100 mW/cm^2} \tag{6}$$

where $G_i = 1000\ W/m^2 = 100\ mW/cm^2$ is the global irradiance incident at the solar cell under standard test conditions. As a result, the power conversion efficiency, or basically the efficiency of the solar cell, gives the fraction of the maximum power delivered by the solar cell at standard test conditions to the power incoming on the solar cell at those same conditions.

As we are also looking at bifacial solar cells, the J-V curve measurements are also performed for the back side of the cells. All the calculations explained above are then also performed for the back side measurements. What is interesting then is to compare the performance of the cell under rear illumination to the performance when the front side of the cell is facing the light source. We can make this comparison through the bifaciality factor, which is defined as follows

$$Bifaciality\ factor\ (bf) = \frac{Rear\ side\ parameter}{Front\ side\ parameter} = \frac{x_{back}}{x_{front}} \tag{7}$$

where the parameters x_{front} and x_{back} can be any parameter calculated from the J-V curve of the front side and back side of the solar cell respectively. In this case this is the short circuit current density, the open circuit voltage, the voltage at maximum power point, the current density at maximum power point, the maximum power, the fill factor, and the power conversion efficiency. This fraction is usually given as a percentage, and it tells us how close the performance of the back side is to the front side, where 100% would mean that the performance parameters are equal. If the bifaciality factor is under one hundred percent this means that the parameter has a higher value (is better) for the front side than for the back side. If the bifaciality factor is higher than one hundred percent it means that the back side is performing better than the front side for the parameter in question.

2.3.5 External quantum efficiency

External quantum efficiency (EQE) does in short give a measure of how effectively the cell converts photons into charge carriers and collects them (Honsberg & Bowden, 2019). That is, as a function of wavelength it gives the percentage of incoming photons that is converted into a collected charge carrier. Accordingly, if a cell for a given wavelength has an external quantum efficiency of 100%, this would mean that for each incoming photon for this given wavelength an electron-hole pair is created and collected. As follows, any value below 100% indicates losses in the solar cells.

The short-circuit current density of the solar cell, which in the previous section was explained could be extracted from the J-V curve, can also be calculated from the external quantum efficiency. It is obtained by integration of the external quantum efficiency over all measured wavelengths as defined by the formula (Almora et al., 2021)

$$J_{sc} = \frac{q}{hc} \int EQE(\lambda) \cdot \lambda \cdot \Gamma_{AM1.5G}(\lambda)\, d\lambda \tag{8}$$

In the formula q is the elementary charge, h is Planck's constant, c is the speed of light, EQE(λ) is the external quantum efficiency as a function of wavelength, λ is the wavelength and $\Gamma_{AM1.5G}$ is the AM1.5G solar spectrum.

2.4 Modelling

Modelling is a useful tool in the research on solar cells, for the simple reason that it allows for the analysis of solar cells without having to actually fabricate and characterise the devices. To illustrate, with thin film solar cells such as antimony selenide based solar cells, the device consists of many layers. Modelling can be used as a tool to investigate if a material is suitable for the application or not, requiring much less work than implementing the material in a physical solar cell. However, the modelling is not entirely independent from experimental work. In order to be able to simulate a material, some knowledge is needed of the material, the necessary parameters needed for the equations used for the simulations. The parameters must then be obtained experimentally. The modelling is also a useful tool to investigate how the performance of the device is dependent on these parameters, as a sensitivity can easily be obtained by varying the value of the parameters and seeing how it affects the performance. It can also be used to optimise aspects of the solar cells, such as the thickness of the different layers.

Some papers have been published utilising modelling as a tool to analyse antimony selenide based solar cells. Efficiencies of 16.5 % (Lin et al., 2018), 13.2 % (Baig et al., 2019) and all the way up to 28.25 % (Mamta et al., 2022). This illustrates a further potential of improved efficiencies for antimony selenide based solar cells beyond the current record efficiency. These reports all utilise SCAPS software for the simulations, while I will in this thesis use Silvaco. These papers considered monofacial cells, and no modelling work on bifacial antimony selenide based solar cells is known.

Electrons excited to the conduction band are not in a stable state, and unless the electron is collected by the p-n junction it will recombine with a hole on the valence band. The recombination is for the modelling assumed to be solely caused by Schockley-Read-Hall (SRH) recombination (Honsberg & Bowden, 2019). This is recombination via defects in the band gap. The most efficient defects for SRH recombination in the middle of the band gap is assumed. The SRH recombination is depending on the lifetime of the carriers. The lifetime gives the average time a photogenerated carrier exist before it recombines. An electron lifetime of 67 ns have been reported for antimony selenide (Chen et al., 2017). Related to the lifetime is the diffusion length which gives the average distance a photogenerated carrier can cover before recombining. With the 67 ns electron lifetime, a diffusion length of 1.7 μm was reported (Chen et al., 2017). What this means is that if for instance an electron hole pair is generated close to the p-n junction, and the thickness of the absorber is more than the diffusion length, the hole would on average not be collected as it has to reach the back contact. Considering how this affects the optimal thickness of the absorber, if the absorber is too thin the amount of absorbed light will be reduced. This comes back to the absorption coefficient, and the fact that a certain width of the material is needed to completely absorb the light. Too thin a material and some light will actually pass through it, making it transparent to certain wavelengths. On the other hand, by making the absorber too thick the limiting factor is recombination. Charge carriers cannot travel longer than the diffusion length before recombining. When electron hole pairs are created in the absorber, they must be collected by the electrodes in order for the solar cell to give a current. If the absorber is too thick carriers will not be able to reach the electrodes and there will be a loss of current and efficiency. As a result, the optimisation of width is the balance of recombination and the amount of absorbed light.

Both the front and back contacts of the solar cell is modelled as Schottky contacts, a metal-semiconductor junction (Streetman & Banerjee, 2016, pp. 251-255). The metal-semiconductor junction can either be rectifying or non-rectifying. Whether the junction is rectifying or not depends on the work functions of the semiconductor and the metal. For a metal-semiconductor junction with a p-type semiconductor, the junction will be rectifying if the work function of the semiconductor is higher than the metal work function. In this case the rectifying junction limits the flow of holes from the semiconductor to the metal. This will reduce the collection of the photogenerated carriers in the solar cell, making the solar cell less efficient. On the other hand,

a non-rectifying, or ohmic, contact occurs when the semiconductor work function is smaller than the metal work function. In this case the holes can easily pass from the semiconductor to the contact, which is preferred for the solar cell.

3 Methods

The work in this thesis can be divided into three main parts. Fabrication of the solar cells, the characterisation of the materials and the solar cells, and the modelling of the solar cells using Silvaco. This section describes the methods and steps procedure used to perform the work in each of these parts. The main parts themselves are summarised below. First the solar cell itself is explained. The fabrication of the solar cells was the first main task, it consisted of the following steps:

1. Preparation of glass/FTO substrate
2. Deposition of the titanium dioxide buffer
3. Deposition of the antimony selenide absorber
4. Deposition of the P3HT hole transport layer
5. Deposition of the back contact
6. Preparation of bifacial samples with ITO back contact

After this the methods used for characterisation of materials and the solar cells is explained. Once the solar cells were finished their performance could be assessed through:

1. J-V characterisation of the solar cells
2. External quantum efficiency (EQE) measurements of the solar cells

Some of the individual materials of the solar cells were characterised as well:

1. XRD of antimony selenide (the sample used is the solar cell without the back contact)
2. UV-Vis of antimony selenide and P3HT (antimony selenide on roughened glass and P3HT on glass)
3. Hot probe measurement of antimony selenide

Finally, the modelling using Silvaco is described.

1. Optimisation of thickness
2. Optimisation of doping
3. Sensitivity analysis of the buffer doping

4. Sensitivity analysis of the charge carrier lifetime
5. Introduction of hole transport layer
6. Simulation of bifacial cell

The theoretical background for the methods is previously described in the theory and literature section. The applicable theory will be referenced as it is applied in this section.

The fabrication and characterisation of the solar cells were performed at Tallinn University of Technology (TalTech). While I was able to participate in parts of the fabrication process of the solar cell to watch and learn, the samples used for the characterisation are not fabricated by me. Due to the complexity of the different fabrication steps and the level of knowledge and familiarity required to operate the machines, me making the solar cells individually was not in the scope of this thesis. Several people were also involved in the different steps of the fabrication, having specialised in a method or having worked more with that particular material. Despite this I was able to participate, and for some parts do some individual work, on the preparation of the substrates and the deposition of the buffer, absorber and hole transport layer.

3.1 Fabrication

The solar cells are fabricated in a superstrate configuration. What is meant by a superstrate configuration is that the fabrication starts with the front side of the solar cell, and the deposition of the back contact is the final step. This section will go through each of the layers of the reference solar cell, consists of the glass substrate, the FTO transparent electrode, the TiO_2 buffer layer, the Sb_2Se_3 absorber layer and the gold back contact. In addition to this, the P3HT hole transport layer and the back contact for the bifacial samples will be considered.

This section will go through the different layers in the solar cells and describe how the antimony selenide based solar cells were fabricated. In order to compare the different changes made, such as inclusion of the hole transport layer or the bifacial cell design, samples with similar performance was needed. Therefore, the samples were chosen based on performance, and for that reason not every single one of the samples have the exact same fabrication process. The same methods are used for all the samples, but differences occur for some of the parameters of the method, for example, substrate temperature in USP and temperature gradients between the source and substrate in CSS. However, as the focus was the investigation of the use of hole

transport layer and the design of bifacial solar cells, and not the optimisation of the fabrication procedure, this is not of importance. The most important thing was to ensure comparability between the cells.

3.1.1 Glass and transparent electrode

With the superstrate configuration, the substrate for the fabrication is the glass on the front side of the solar cell. In this case glass precoated with FTO is used so the substrate actually consists of the glass and the transparent electrode. The substrate is prepared by cutting it into the desired size and clean it to remove any contamination. Two different CSS set ups are used for the deposition of the absorber layer, so the size of the substrate depends on which of the set ups were used. Thus, the size of the substrate is either 25 mm times 25 mm or 30 mm times 30 mm. After cutting the substrate into the desired size it was cleaned using the following procedure. First the substrate is wiped with ethanol. Then the substrate was kept in a solution of 10g potassium dichromate ($K_2Cr_2O_7$), 10mL water H_2O and 100mL sulphuric acid (H_2SO_4) for 30 minutes. After the 30 minutes have passed the substrate is removed from the solution and any solution remaining on the substrate is rinsed off using deionised water. The substrate is then placed in deionised water and brought to a boil. Once boiling the substrate was removed from the plate and let cool. Finally, once the substrate has cooled down it is air dried using a heat pistol. Once this procedure is completed the substrates are ready for deposition of the buffer layer.

3.1.2 Buffer layer

The buffer is deposited on the side of the substrate which is coated with FTO. When depositing the buffer, a thin stripe on two parallel sides of the substrate is masked so that access to the FTO is ensured after the deposition of the buffer. As the FTO is the front contact access is important as to connect the solar cell to the external circuit for measurements. The accessibility of the front contact must also be considered for the subsequent layers. The buffer is deposited using a method called ultrasonic spray pyrolysis (USP). 100 mL of a solution of 0.2 M titanium(IV)isoproxide and pentanedione with a molar ratio of 1:1 dissolved in ethanol is used for the ultrasonic spray pyrolysis. The molar ratio of 1:1 means that the mix contains equal amounts of pentanedione and titanium(IV)isoproxide. With the molar concentration (M = mol/L), the molar mass (g/mol) and the total amount of the solution (L) known, we can calculate

the amount of grams of titanium(IV)isoproxide and acetylacetone to be used on the solution by multiplying the three quantities. The method works by placing the sample on a hot plate and spraying the solution on it. The temperature of the hot plate, the substrate temperature, can be adjusted. First a substrate temperature of 360°C and 70 cycles were tried but did not give good results, instead a substrate temperature of 500°C and 85 cycles were attempted. Once the deposition was complete the samples were left to cool down, and once cool the sample was annealed in air for 30 minutes at 460°C.

3.1.3 Absorber

The antimony selenide used as the absorber layer is deposited using a method called close space sublimation (CSS). The CSS deposition is performed in a two steps procedure as explained in the theory section. In the first step a seed layer of antimony selenide is created, while in the second step the main layer is grown on the seed created in the first step. The CSS setup consist of a hollow standing cylinder, the deposition chamber. The antimony selenide powder is placed at the bottom of this cylinder, this is called the source. One centimetre above the source, at the top of the cylinder, the sample is placed facing with the buffer down towards the antimony selenide powder, that is with the front side of the solar cell facing up. Where the samples are placed is called the substrate. For the deposition it is important that the sample is placed so that antimony selenide is only deposited on the buffer layer. No antimony selenide should be deposited on the areas of FTO masked during the deposition of the buffer. At the top and bottom of the cylinder are heating elements and thermocouples located. This setup is an advantage with the close space sublimation method because it makes it possible to control the heating of the source and the substrate individually. The source is heated from below and the substrate from above. The temperature can be read from each of the thermocouples at the source and substrate, making it possible to control the temperature as it is ramped up. The source should have such a temperature so that the antimony selenide powder evaporates, meanwhile the substrate should have a temperature such that the antimony selenide does not reevaporate. A challenge is that because the source has a higher temperature than the substrate it will continue to heat the substrate still after the heating have been stopped. If this heating of the substrate is too high after we have stopped applying heat to both the source and the substrate, it might cause the film deposited at the substrate to reevaporate, which in turn would also destroy the sample. Optimising of the temperatures and ramping of the temperature is, therefore, important to avoid the substrate being heated so much by the source that the antimony selenide film reevaporates.

The close space sublimation method uses vacuum. Once the sample is placed in the deposition chamber, which again is situated within a larger vacuum chamber, vacuum is created in the vacuum chamber. First pre-vacuum is created using a rotary pump, after which a diffusion pump is used in order to reach high vacuum. When high vacuum is achieved the deposition can begin. The temperature during CSS was measured using type K thermocouples, one to measure the temperature of the source and one to measure the temperature of the substrate. When measuring the temperature, it is recorded in units of mV which can be converted to °C. For the seed layer the substrate was heated to 8.3 mV (204 °C) and the source to 15 mV (367 °C) before the heat was turned off. The substrate reached a maximum temperature of 11.75 mW (289 °C) and the source reached a maximum temperature of 16.42 mV (401 °C). Before moving on to deposition of the main layer the system was left to cool down until the temperature had sunken beneath 10 mV (246 °C). For the main layer the substrate was heated to 16.4 mV (400 °C) and the source to 19 mV (461 °C) before the heat was turned off. The substrate and source reached maximum temperature of 17.8 mV (433 °C) and 19.5 mV (473 °C) respectively. Once deposition is complete the sample is left to cool down in the vacuum. Once cool, the vacuum is removed and the sample taken out. The sample is now cut into four equal pieces, each piece making up a corner of the original substrate. By cutting it in this way each piece has access to the FTO.

3.1.4 Hole transport layer

The hole transport layer is only applied for some samples. It is not used on the references or for the bifacial cells where the back contact is applied directly on the absorber. For samples utilizing the hole transport layer, a P3HT hole transport layer is introduced between the absorber and the back contact. P3HT was also deposited on a glass substrate in order to perform UV-Vis measurements to obtain transmittance and reflectance of the P3HT film. For my work I participated in the preparation of the samples used for UV-Vis, but not when P3HT was applied on the solar cells.

The P3HT hole transport layer used here is applied using spin coating. Two different concentrations of P3HT, 1% and 0.5%, are used to apply different thicknesses of the hole transport layer. The 1% concentration giving a thicker film than the 0.5% concentration. The spin coating is performed at 3000 RPM and lasting for 30 seconds. For the samples prepared for UV-Vis measurements a substrate of 15 mm times 15 mm was used. For these samples 50

mL P3HT solution was applied for the spin coating. After the P3HT have been spin coated on the samples it is placed on a hot plate for five minutes at 50°C. The P3HT should only be applied on the absorber, so any P3HT applied anywhere else, also on the sides and backside, is removed using a cotton swab dipped in chlorobenzene. The P3HT has a purple colour when it is applied, the 1% P3HT having a deeper/darker purple colour, while the 0.5% P3HT has a lighter purple colour. The difference in colour is due to the fact that the 1% solution gives a thicker P3HT layer than the 0.5% solution does.

The P3HT must be activated after the spin coating. When activating the P3HT it crystallises, and its colour turns greener. For the activation the sample is placed in a metal plate together with a piece of glass. The piece of glass is used to measure the temperature. This is done by placing a thermocouple on it, the reason for using the glass and not placing the thermocouple directly on the sample with the P3HT is that we want to avoid damaging the P3HT film. The sample is placed in a vacuum chamber, and once high vacuum ($3 \cdot 10^{-4}$ mbar) is reached, a current of about 21 A is passed through the metal plate. The metal plate is resistive so the current passing through it creates heat, which again heats the samples placed on the metal plate. The thermocouple on the glass piece measures the temperature. The samples are heated to 170°C and kept at that temperature for five minutes. After these five minutes have passed the current is switched off and the samples are left to cool in the vacuum. Only when the temperature of the samples has fallen below 50°C are the samples removed from the vacuum and the activation process is complete.

3.1.5 Back contact

For the monofacial cell the material used for the back contact is gold. The gold is deposited on the solar cell through evaporation in vacuum, with a deposition time of four minutes. A mask is used on the samples to make sure that the gold is only deposited on the quarter circle of the sample where we have the absorber layer and hole transport layer. For the bifacial cells, instead of gold, ITO is used as the back contact. This is simply because gold is not transparent, and so instead ITO is used which is a transparent conductive oxide (TCO), similar to FTO used for the front contact. For some of the bifacial samples, however, a thin layer of gold is included between the absorber and the transparent back contact. The ITO for the bifacial cells is

deposited using sputtering. The thin gold layer is deposited using the same method as for the monofacial samples.

After deposition of the back contact the solar cell is practically complete, however, one step remains, and that is the scribing of the solar cells. The scribing is basically that the solar cell is separated into several smaller solar cells, although, still situated at the same substrate, the glass. This is done by cutting through the back contact, HTL, absorber and buffer so that when only one scribed cell is connected to the external circuit only charge carriers from this cell will be collected. When connecting the solar cell to a circuit it is connected at the front contact, the FTO which we made sure was not covered completely by the different layers, and the back contact. Thus, despite being called front and back contact, both contacts are accessed from the back side of the solar cell.

3.2 Material and solar cell characterisation

The characterisation can be divided into two categories. One is the characterisation of the materials, where work is done mainly on the antimony selenide absorber and the P3HT hole transport layer. The second is the characterisation of the solar cells. There are two main measurements when it comes to the characterisation of the solar cell, they are external quantum efficiency and J-V curve measurements. These are two of the most important measures of the performance of a solar cell.

This thesis is considering both monofacial and bifacial solar cells. As bifacial solar cells can be illuminated from both sides, and it is not expected that the performance is equal under front and rear illumination, the J-V and external quantum efficiency measurements are performed from both the front side and the back side of the solar cells. While measurements from the backside is mainly interesting for the bifacial solar cells, by measuring all cells in this way it enables us to do some interesting comparisons of the performance. We can compare how different cell perform from the front and the back, but we can also compare how each cell perform from the backside compared to the front side. A good method to compare the performance of the backside of the solar cell to the performance of the front side of the solar cell is through what is called bifaciality factor and is simply the fraction of a parameter from the back side to the

corresponding parameter from the front side. This fraction gives a percentage which tells us how equal the performance of the back side is to the performance of the performance of the front side. For the J-V and EQE measurements the back side of the solar cell is not illuminated for the front side measurements, while for the back side measurements the front side is covered from illumination. However, the sides of the cell and the areas outside the active area is not covered. When not covering the sides and the areas outside the active area light is allowed to enter the cell through these areas and contribute to electron-hole generation. The area of the cell, used to calculate the current density, is the area of the back contact, both for front side and back side measurements, as this is the active area which collects holes. The probes used for connecting the solar cells during measurements are placed on the back side of the solar cell, both for the back contact and the front contact. This is an advantage when doing frontside measurements, having access to both contacts from the backside, and is really a consequence of the superstrate configuration. However, for measurements from the back side this is causing some challenges. First of all, the measurement equipment was not perfectly suited for back side measurements. This was, however, easily solved by moving the probes from the back to the front of the sample holders. Having the probes placed on the illuminated side of the solar cell would cause some shadowing of the device. In the case of the probe placed on the front contact this was not an issue as the front contact was on the side of the device outside the active area of the cell, therefore, no shadowing was caused. The probe for the back contact, on the other hand, was placed directly on the active area of the cell, covering part of the ITO which is the window for the light to enter the p-n junction. The probe was also not placed directly on a sample, but a small piece of indium was placed inbetween to prevent the probe from scratching the ITO and damaging the solar cell. To take the shadowing into account the area of this indium pad was subtracted from total area of the cell, this was then used as the area when calculating the current density.

3.2.1 Ultraviolet-visual spectroscopy

Ultraviolet-visual spectroscopy (UV-Vis) measurements are used to obtain the transmittance and reflectance of the antimony selenide semiconductor, and 0.5% and 1% P3HT. The UV-Vis measurements are made using a setup with a Jasco V-670 Spectrophotometer equipped with an ISN-723 integrating sphere. The UV-Vis measurements cannot, however, be performed on a finished solar cell, the materials to be measured must be deposited a transparent substrate

(Carron et al., 2019). Hence, the samples used for the UV-Vis measurements is a film of antimony selenide deposited on roughened glass and P3HT deposited on glass.

With the measurements of transmittance and reflectance completed, the absorption coefficient is calculated using equation 1**Error! Reference source not found.**. To use this equation to find the band gap the thickness of the semiconductor film must be known. However, as we do not know the thickness of the films, through some simple manipulations based on assuming that the thickness is constant, which it anyways is assumed to be, the same method can be adapted so that it still can be used to extract the band gap without knowing the thickness. Without knowing the thickness of the semiconductor film, the absorption coefficient cannot be calculated, but the absorption coefficient multiplied with the thickness can, which can still be used to extract the bandgap as it is only multiplied by a constant. From

$$\alpha = \frac{1}{d}\ln\left(\frac{1-R}{T}\right) \tag{9}$$

we can multiply with the thickness d on both sides of the equation and get

$$\alpha d = \ln\left(\frac{1-R}{T}\right) \tag{10}$$

From the absorption coefficient multiplied with the thickness the band gap can be calculated given the relation in equation 2 which is

$$(\alpha h\nu)^{\gamma} = A\left(h\nu - E_g\right) \tag{11}$$

To use this equation with αd for finding the band gap we must multiply both sides by the thickness raised to the power of γ, d^{γ}, which is a constant. This gives us

$$(\alpha h\nu)^{\gamma} d^{\gamma} = A d^{\gamma}\left(h\nu - E_g\right) \tag{12}$$

$$(\alpha d h\nu)^{\gamma} = A d^{\gamma}\left(h\nu - E_g\right) \tag{13}$$

Where we now can use αd as given above. For finding the bandgap we plot the left-hand side, $(\alpha d h\nu)^{\gamma}$, as a function of photon energy, $h\nu$, and finding the value of $h\nu$ where $(\alpha d h\nu)^{\gamma}$ is equal to zero

$$(\alpha d h\nu)^{\gamma} = 0 \tag{14}$$

Why this is so is easily seen by setting the right-hand side of the equation above equal to zero as well. For the right-hand side we then have

$$Ad^{\gamma}\left(h\nu - E_g\right) = 0 \tag{15}$$

Ad^{γ} is a constant, so we can divide by it on both sides of the equation. This gives

$$h\nu - E_g = 0 \tag{16}$$

$$E_g = h\nu \tag{17}$$

where $(\alpha d h\nu)^{\gamma} = 0$. Which shows that the bandgap is given by the energy $h\nu$ for where $(\alpha d h\nu)^{\gamma}$ is equal to zero. What this basically tells us is that the photon energy which gives an absorption coefficient times the thickness of the film of zero, $(\alpha d h\nu)^{\gamma} = 0$, has the same energy as the band gap. With this method we do not need to know the thickness of the film in order to determine the bandgap.

What is clear once we have the plot is that $(\alpha d h\nu)^{\gamma}$ does not have a clearly defined point where it becomes zero. Meaning that we cannot simply find the zero point and extract the corresponding $h\nu$ value as the band gap. But the curve has two distinct features which can help us find the band gap. The first of these features is that for small enough $h\nu$ the values for $(\alpha d h\nu)^{\gamma}$ is practically equal to zero. The second feature is that after, for higher values of $h\nu$, this practically equal to zero part of the plot there is a segment of the graph where $(\alpha h\nu)^{\gamma}$ is increasing approximately linearly. Based on this, the following method is used to extract the band gap. First a linear fit such as

$$y = ax + b \tag{18}$$

where $y = (\alpha d h\nu)^{\gamma}$ and $x = h\nu$ is made of this approximately linearly increasing segment. Here a is the slope and b is the intercept with the y-axis. We want to find the value of $h\nu$ where $(\alpha d h\nu)^{\gamma}$ is zero, so we have to find the intercept with the x-axis. This intercept is then given when

$$y = (\alpha h\nu)^{\gamma} = 0 \tag{19}$$

Solving for the right-hand side of equation 19

$$ax + b = a \cdot h\nu + b = a \cdot E_g + b = 0 \tag{20}$$

$$E_g = -\frac{b}{a} = -\frac{intercept\ with\ y-axis}{slope} \tag{21}$$

Which gives the bandgap of the semiconductor. Because antimony selenide is an indirect semiconductor, we have to use $\gamma = 1/2$ to find the band gap. But we can also use $\gamma = 2$ to find the smallest direct transition between the valence band and conduction band as well. P3HT is a direct semiconductor so we use $\gamma = 2$ when finding the band gap.

3.2.2 Hot probe

The hot probe method is used to determine the conductivity type of antimony selenide. For the experiment three different materials were tested. The materials tested in addition to antimony selenide were tin sulfide (SnS) and bismuth sulfide (Bi_2S_3). Tin sulfide known to have p-type conductivity and bismuth sulfide known to have n-type conductivity were used as references for the measurement of antimony selenide. By comparing the results from the measurements of the references we can determine whether the antimony selenide film is p-type or n-type based on which reference it shows similarities to.

The experiment was conducted by placing the two probes on the sample. The probes are connected to a multimeter and is used to measure the voltage built up between the cold and the hot probe. The probe being heated is connected to the positive terminal of the multimeter. The data is recorded by filming the multimeter as heat is applied to the probe. The data is then extracted from the film by going through frame by frame and writing down each change of voltage on the multimeter and the time of the change. This gives the voltage as a function of the time that the heat has been applied. Ideally, we would have voltage as function as temperature, but the set up did not allow for the measurement of temperature. However, as we are applying heat and measures the voltage as a function of time, it is clear that the temperature itself would be a function of time (it would increase as time passes) and, therefore, having time as the x-axis instead of the temperature still gives the same picture of the conductivity type of the sample.

3.2.3 XRD

X-ray diffraction measurements are performed using a Rigaku Ultima IV x-ray diffractometer. The XRD is measured for angles between 10° and 80°. The sample measured is an antimony selenide solar cell just without a hole transport layer and the back contact. The layers of sample thus being antimony selenide deposited on the TiO_2 buffer which was deposited at the FTO coated glass. In the XRD measurements the material beneath the antimony selenide might actually show up in the data. So why don't we perform the XRD on a sample without these layers, for example, antimony selenide deposited directly on glass? This seems advantageous as we would avoid the other materials creating noise in the XRD picture from the antimony selenide. However, the structure of the antimony selenide film is altered by the substrate on which it is deposited. As a result of this, antimony selenide on glass and antimony selenide on titanium oxide might give different results. This is the reason for making the sample as if it was to be used as the actual cell.

The measurements gives the intensity of the diffraction in units of counts per second (cps) as a function of the angle between the incoming and reflected x-ray (2θ). The measured data exhibits nonzero values between the peaks, especially for small angles. Due to this, a baseline is extracted from the data, which is then subtracted to give the peaks normalised to zero. Further the peaks and the corresponding angles can be compared to values reported in the literature in order to assess the crystal structure of the semiconductor.

3.2.4 Current density – voltage curve

The current density – voltage correlation is measured using a Wavelabs LS-2 solar simulator and a Autolab Potentiostat/Galvaniostat, this is the same setup as the one used in the paper by Krautmann et al. (Krautmann et al., 2021). In fact, it is the I-V curve that is measured, the current density is calculated from the measured current after the measurements. From the measurements with get the current from the solar cells as a function of voltage. Having obtained the J-V curve of a solar cell, the short circuit current density, open circuit voltage, maximum power, short circuit current density at maximum power point, voltage at maximum power point, fill factor and power conversion efficiency is extracted from this data. These parameters are extracted from the J-V curve data using Origin. The only additional parameter that is needed is

the power of the incident light, which for standard test conditions are 100 mW/cm^2. This section will describe the methods used to calculate the parameters mentioned here.

The first thing we need to consider is the units of the data. From the J-V measurements we have the voltage in units of Volts (V) and the current in the units of Amps (A). For the following calculations we want the voltage to be in units of V and current in the units of mA. The voltage is already in Volts so no conversions are needed. For the current, however, we need to convert from A to mA. This is an easy calculation done simply by multiplying the current in Amps by 1000 to get the current in mA. An important consideration is that the current, I, given by a solar cell is a function of the size of the solar cell. The larger the cell is, the more light can be collected by it. Consequently, more photogenerated carriers are generated, which results in more current. Now if all the cells were made in a standard size this would not be a problem. However, solar cells can come in many shapes and sizes, and because of this current cannot be compared between the cells and comparison of performance is, thus, not possible when it comes to current. As other performance indicators such as fill factor and power conversion efficiency is calculated from the current, this will also affect these. To solve this problem, we are considering the current density, J, instead of the current. The current density is just the current produced by the cell divided by the contact area of the cell. Doing this allows us to compare how much current, per area, different cells produce. This enables us not only to compare the cells in this work, but also any other solar cells where the current density is given. So, for each cell the contact area is measured, and the current density in mA is divided by the area in cm^2. Thus, we have the current density given in mA/cm^2. When the J-V curves are measured it is measured both in the dark and under illumination. The parameters mentioned above is calculated from the illuminated measurements. The dark- and light-current must be separated from each other. From the light-current and voltage the power per area is calculated from equation 3 with units $V \cdot mA/cm^2 = mW/cm^2$. Directly from the J-V curve we find the short circuit current density and open circuit voltage by finding the point where the curves cross the y-axis (x=voltage=0) and x-axis (y=current=0) respectively. In short circuit we have no voltage, so the current is given when the voltage is equal to zero. Similarly for open circuit we have no current, the current cannot flow without a closed circuit, so the voltage is given when the current is zero. Because of the discrete nature of the measurements, no single measurement corresponds to x=0 or y=0. Therefore, we cannot simply pick the values for open circuit voltage and short circuit current density out from the measurements. To approximate the parameters, we use linear

regression. Four measurement points are used for the linear regression. For short circuit current density, we take the two first measurement points for x>0 and the two for x<0. For the open circuit voltage, we use the two first measurement points for y>0 and y<0. The result of the linear regression is a standard linear function of the form

$$y = ax + b \tag{22}$$

where a and b are constants, x is the voltage and y is the current density. Hence, we can write

$$J = a \cdot V + b \tag{23}$$

where a and b are calculated in the linear regression. Following this, all we need to do is set either current density or voltage equal to zero and solve for the other one. The short circuit current density is given by

$$V = 0 \tag{24}$$

$$J_{sc} = a \cdot 0 + b = b \tag{25}$$

and the open circuit voltage is given by

$$J = 0 \tag{26}$$

$$0 = a \cdot V_{oc} + b \tag{27}$$

$$a \cdot V_{oc} = -b \tag{28}$$

$$V_{oc} = -\frac{b}{a} \tag{29}$$

It is important to remember that a and b are different for the short circuit current density and the open circuit voltage. The maximum power point (MPP) is simply found by finding the point where the power reaches is maximum. Then by finding the voltage that corresponds to this maximum power the current density at maximum power point is easily extracted from the J-V curve. Having all these parameters, the fill factor and power conversion efficiency can be calculated using equation 4 and 5 respectively.

3.2.5 External quantum efficiency

External quantum efficiency (EQE) is measured by illuminating the solar cells with light as a function of wavelength and measuring the short circuit current for each wavelength. The EQE

measurements are performed for wavelengths from 300 nm to 1100 nm. Once more, with the same measurement setup as used in the paper by Krautmann et al. (Krautmann et al., 2021), the sample is illuminated with a monochromatic light obtained using a Newport Cornerstone 260 monochromator (model 74125) while a Newport Oriel Merlin Lock-In Digital amplifier is used for detection. Similarly to the J-V curve measurements when measuring the external quantum efficiency, we get the results calculated from the current and not the current density, which it is supposed to be. This means that the obtained data must be divided by the contact area of the cell in order to give the actual external quantum efficiency.

Two important parameters can be extracted from the external quantum efficiency (EQE). Firstly, we can calculate the short circuit current density and compare this with the short circuit current density calculated from the J-V curves. Secondly, the band gap can be extracted from the external quantum efficiency. This can be compared both to values from the literature and results from the UV-Vis measurements. We can start by looking into how the short-circuit current density (J_{sc}) can be calculated from the external quantum efficiency. This is done as defined in equation 7, the AM1.5G light spectrum used is from NREL (NREL, n.d.). The integration is performed numerically using the built-in integration function in Origin. The resulting short circuit current density should in theory be equal to the short circuit current density calculated from the J-V curves. As the external quantum efficiency measurement setup needed calibration before doing the measurements, we used this method to calibrate the instruments. By measuring the external quantum efficiency, we could calculate the short circuit current and compare this to the already obtained short circuit current density from the J-V curve. Based on this we could increase or decrease the gain on the instruments depending on whether the short circuit current from the external quantum efficiency was too low or too high respectively. This procedure was repeated until a good agreement between the two measurements was achieved. This, however, means that nothing can be said about how the two measurements compares for the sample used for the calibration. For subsequent measurements, however, we can examine the relation between the two. The sample used for the calibration was not one of the samples used for the results here.

The band gap of the antimony selenide absorber can be extracted from the external quantum efficiency of the solar cell by plotting $(E \cdot EQE)^2$ as a function of the energy E (Carron et al., 2019). The wavelengths are transformed into energies using

$$E = \frac{hc}{\lambda} \tag{30}$$

1. At the lower left region of the plot there is a linear region. This is between where the plot flattens to the left and the kink in the graph above to the right. Select a portion of this linear area and make a linear fit.
2. From the linear fit we get the slope and the intercept with the y-axis which corresponds to a and b respectively in

$$y = ax + b \tag{31}$$

3. The bandgap is found where this linear function crosses the x-axis (y=0). So the bandgap is given by

$$E_g = x_{y=0} = -\frac{b}{a} = -\frac{intercept\ with\ y-axis}{slope} \tag{32}$$

The raw external quantum efficiency data is noisy and thus the curve is smoothed in order to ease the calculations of the band gap. After the smoothing, any negative external quantum efficiency values are set to zero. This is because the external quantum efficiency cannot be zero. It gives the number of collected charge carriers as a function of incoming photons, and a negative value would mean that a photon does not create a charge carrier, but destroys one, which is not possible.

3.3 Modelling

Both monofacial and bifacial antimony selenide based solar cells, with and without hole transport layer, is modelled. These simulations are performed using Silvaco TCAD. The main part of the Silvaco software utilised for these simulations is the Atlas semiconductor simulator. The two main tools in the Atlas simulator used is the Blaze: Compound Material 2D simulator (Silvaco, 2019, pp. 484-565) and Luminous: Optoelectronic Simulator (Silvaco, 2019, pp. 642-729). Blaze is used to model the heterojunction between the CdS buffer and the Sb_2Se_3 absorber, and also the junction between Sb_2Se_3 and P3HT for the samples utilising the hole transport layer. Luminous is used to simulate light propagation and absorption in the solar cell. The focus

of the modelling is on the development of a bifacial antimony selenide based solar cell, implementation of P3HT hole transport layer and the optimisation of thickness and doping of the antimony selenide absorber. Additionally, the simulations have been performed to analyse the effect on the solar cell efficiency of the free charge carrier concentration of the CdS buffer, the charge carrier lifetime and the thickness of the absorber at high doping concentration.

A script is written that defines the modelling in Silvaco. In the script the structure of the solar cell and the material parameters is defined, in addition to the characterisation methods and the parameters to extract from the results. The transfer matrix method is used to model the propagation of light in the device (Silvaco, 2019, pp. 657-659). When characterising the solar cells, they are illuminated by AM1.5 solar spectra (Silvaco, 2019, p. 723) which is similar to the standard test condition used for the experimental characterisation. A voltage sweep from 0 V to 1 V in steps of 0.01 V is applied. From this the J-V curve of the solar cells is obtained, and the performance parameters of the solar cells are calculated from the J-V curve in the same way as for the experimental results as explained in section 3.2.4.

3.3.1 Device structure and material parameters

The reference device structure used for the modelling is the monofacial cell without a hole transport layer. This monofacial solar cell consist of a 200 nm ITO front contact, 100 nm CdS buffer, antimony selenide and a 100 nm gold back contact. The thickness of ITO and CdS is taken to be the same as for the transparent electrode and buffer the paper by Spalatu et al. (Spalatu et al., 2021). All layers are assumed to have a constant thickness except for the absorber. The thickness of the antimony selenide absorber will be optimised through the modelling. ITO, CdS and gold are all materials which are predefined in Silvaco, easing the implementation of the solar cells. Sb_2Se_3 and the hole transport layer P3HT, are not, and must be manually implemented as new materials into the program. The new materials are implemented by using another semiconductor as a basis, and then changing any parameter to correspond to the new material. Which material used as a material does not matter as long as all material parameters are changed to correspond to the new material. The necessary parameters for the new materials to be implemented is found in the literature. Table 1 summarises the parameters for antimony selenide which is taken from the literature and used for the simulations. Similarly to Sb_2Se_3, P3HT is not a predefined material in Atlas. All the

parameters as used for Sb_2Se_3 must also be defined for P3HT, except for the electron and hole lifetime as the recombination is not modelled in the HTL similarly to the buffer. The data used for the P3HT is taken from the literature (Dadhich et al., 2021). Despite ITO, gold and CdS being predefined materials, some additional parameters are needed. These are the free carrier density of CdS, which is set to 10^{18} cm^{-3} (Huang et al., 2015). The free carrier density of the CdS, Sb_2Se_3 and P3HT is implemented by setting the doping level equal to the reported free carrier densities. The front and back contacts is the electrodes of the device. By default in Atlas, the junction between a semiconductor and an electrode is modelled as ohmic, so in order to take the interfaces between the semiconductors and metal into consideration the work function of the metal must be defined. By defining a work function the junction is modelled as a Schottky contact. (Silvaco, 2019, p. 72) The work function of ITO and gold is 4.6 eV (Liu et al., 2016) and 5.1 eV (Mavlonov et al., 2020) respectively.

Important for the modelling is the complex index of refraction. The real component of the complex index of refraction is used to model light intensity in the device, while the complex component is used to model absorption in the device (Silvaco, 2019, p. 645). Therefore, the complex index of refraction as a function of wavelength, to model how the materials react to different wavelengths of light, is needed. For ITO, CdS and gold this data is already available in the software. For the user defined materials, Sb_2Se_3 and P3HT, this data must be provided. Complex index of refraction for P3HT is taken from (Hrostea et al., 2020), and complex index of refraction for Sb_2Se_3 from (Chen et al., 2015). The complex index of refraction for both P3HT and Sb_2Se_3 were digitized from the graphs in the literature.

Table 1: Material parameters used to define antimony selenide in the simulations.

Parameter	**Value**
Bandgap	1.03 eV (Chen et al., 2015)
Electron affinity	4.15 eV (Baig et al., 2019)
Relative dielectric constant	14.5 (Baig et al., 2019)
Valence band density of states	1.86×10^{18} cm^{-3} (Baig et al., 2019)
Conduction band density of states	6.926×10^{18} cm^{-3} (Baig et al., 2019)
Electron mobility	16.9 cm^2/Vs (Chen et al., 2017)
Hole mobility	2.59 cm^2/Vs (Chen et al., 2017)
Electron lifetime	67 ns (Chen et al., 2017)
Hole lifetime	67 ns (Chen et al., 2017)
Free carrier density	1.8×10^{13} cm^{-3} (Chen et al., 2017)

3.3.2 Modelling step by step

The modelling work consisted of many different simulation runs. This section summarise each of them.

1. Optimisation of absorber thickness

   The first step was to optimise the thickness of the antimony selenide absorber. The simulation is performed on the reference monofacial cell. Every parameter is assumed to be constant as defined above, except for the absorber thickness. The simulation performed for thicknesses between 0.1 μm and 3.0 μm. The optimal thickness is used as the reference solar cell for the other simulations.

2. Optimisation of absorber doping

   The optimal doping level of the absorber was investigated by, once more, considering the reference monofacial cell. All parameters were held as in the step above except for the absorber doping. The thickness set as the optimal value as found in the previous step. The simulation performed for absorber doping densities of ranging from 10^{12} cm^{-3} to 10^{16} cm^{-3}.

3. Thickness of absorber at 10^{16} cm^{-3} doping density.

   It is stated in the literature that the optimal doping density for the absorber layer in the solar cell is in the order of 10^{16} cm^{-3} (Chen et al., 2017). However, it was found in the second simulation that using the optimal thickness and optimal doping density did not give the highest power conversion efficiency. Therefore, this additional step was performed, investigating if the optimal thickness is different for a higher doping level. The thicknesses investigated was ranging from 0.2 μm to 5.0 μm. Again, the simulations were performed using the default monofacial cell, with a doping density of 10^{16} cm^{-3} and varying the thickness of the absorber, while keeping the other parameters as default.

4. Sensitivity of carrier lifetime

   Considering the reference monofacial cell once more. The effect of carrier lifetime was investigated by performing the simulation for lifetimes of 10^{-5}, 10^{-6}, 10^{-7}, 10^{-8} and 10^{-9} s. Electron and hole lifetime is assumed to be equal, as it is for the reference case as well. The other parameters were kept as for the reference sample, but the optimal thickness found in step one was used.

5. Sensitivity of the buffer doping

   The carrier density of the CdS buffer has been reported to be in order of 10^{18} cm^{-3} as reported by (Huang et al., 2015). This value is used for the reference sample and all other simulations as well. However, as both lower and higher values have been reported, it is interesting to investigate the effect the buffer doping has on the efficiency of the solar cell. Carrier concentration as low as in the order of 10^{12} cm^{-3} have beem reported (Liu et al., 2010) while carrier concentrations as high as in the order of 10^{19} cm^{-3} have been reported (Kose et al., 2010). Based on this the sensitivity of the efficiency of the solar cell on buffer carrier concentration is investigation by performing the simulations for different carrier concentrations. The reference sample with the optimum absorber thickness is used, running the simulations for absorber doping densities ranging from 10^{12} cm^{-3} to 10^{19} cm^{-3}.

6. Introduction of P3HT hole transport layer.

   A P3HT hole transport layer, similar to the one in the experimental part, was introduced between the absorber and the back contact. The effect of the thickness of the HTL is investigated by running the simulation for thicknesses of 0.001, 0.005, 0.01, 0.02, 0.03,

0.04 and 0.05 μm. The other parameters are as for the reference, with optimal thickness and intrinsic carrier concentration.

7. Bifacial solar cell.

   The final step is to simulate the bifacial solar cell. For this the 0.1 μm gold back contact is replaced by a 0.2 μm ITO back contact. The bifacial cell characterised under illumination from both the back side and the front side, and simulated both with and without the P3HT hole transport layer. The parameters are kept constant for the other layers. Using optimal thickness for the absorber and intrinsic carrier concentration. The P3HT HTL used a thickness of 0.02 μm.

   As a reference, the monofacial cell is simulated from the back side as well.

   For the bifacial sample both with and without P3HT, the effect of the work function of the ITO back contact is investigated by simulation with the actual 4.6 eV work function of ITO, with the back contact assumed to be ohmic and for two higher work functions of 5 eV and 6 eV.

4 Results and discussion

4.1 Samples

Several samples were prepared for the different experiments, some samples even gave several solar cells by scribing the samples. This is the case with the 13L1 bifacial cell and the 13S1 monofacial cell, both giving a regular sized cell and a cell with a small contact area. Table 2 provides a summary of the names of different samples, whether they are monofacial or bifacial and the structure of their layers.

Table 2: Summary of the solar cell samples and their structure.

Sample		**Layers**
13L1 (small contact)	Bifacial	Glass|FTO|TiO2|Sb2Se3|Gold|ITO
13L1	Bifacial	Glass|FTO|TiO2|Sb2Se3|Gold|ITO
13S (bifacial)	Bifacial	Glass|FTO|TiO2|Sb2Se3|ITO
14L1	Bifacial	Glass|FTO|TiO2|Sb2Se3|Gold|ITO
13S_ref	Monofacial	Glass|FTO|TiO2|Sb2Se3|Gold
13S1	Monofacial	Glass|FTO|TiO2|Sb2Se3|P3HT 1%|Gold
13S1 (small contact)	Monofacial	Glass|FTO|TiO2|Sb2Se3|P3HT 1%|Gold
14S_ref	Monofacial	Glass|FTO|TiO2|Sb2Se3|Gold
14S1	Monofacial	Glass|FTO|TiO2|Sb2Se3|P3HT 0.5%|Gold

4.2 UV-Vis

The UV-Vis measurements were used to calculate the band gap of P3HT and both direct and indirect band gap of antimony selenide.

4.2.1 Antimony selenide

Figure 2 gives the reflectance and transmittance, both in percentage, resultant from the UV-Vis measurements of antimony selenide. From these measurements the absorption coefficient times the film thickness, is calculated using equation 10. This is then used to calculate the band gap of the semiconductor. We see that both the reflectance and transmittance exhibit a steep increase starting at about 1000 nm. 1000 nm corresponds to 1.24 eV, which is not far from the band gap of the material. For longer wavelengths, that is lower energies, both the reflectance and transmittance is high. The high transmittance for energies lower than the band gap is expected as this light cannot be absorbed. For energies higher than the band gap the transmittance is close to zero, which indicates that the light that is not reflected is in fact absorbed.

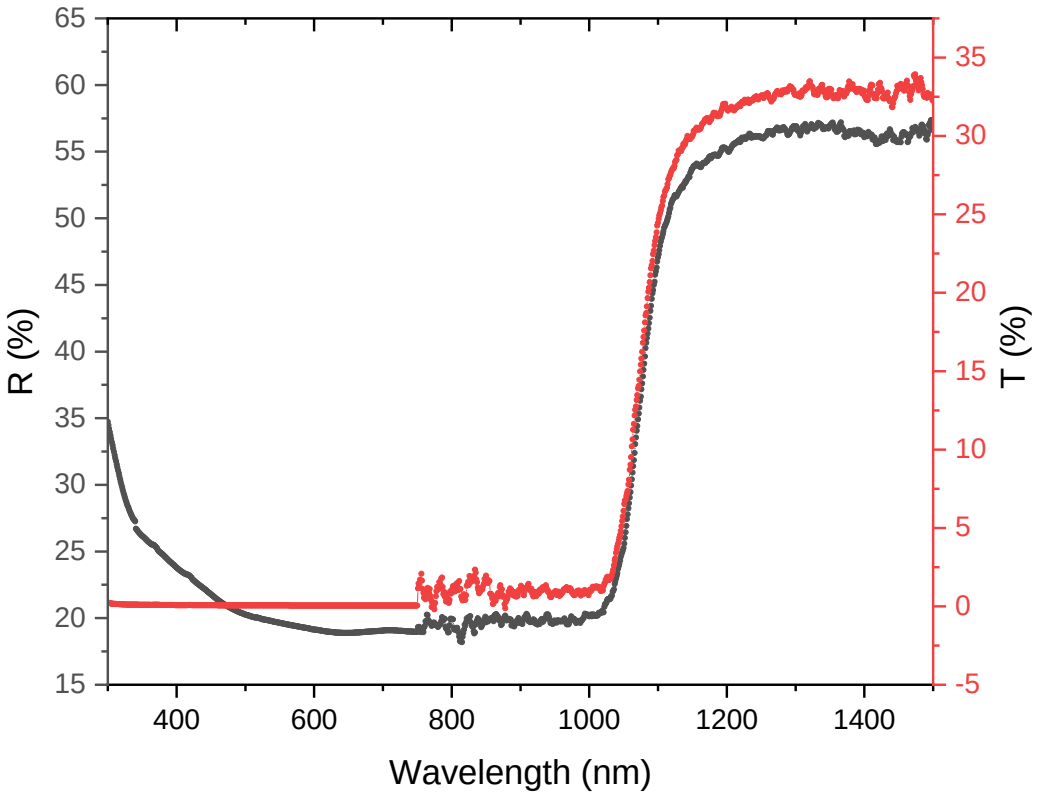

Figure 2: Reflectance and transmittance of antimony selenide (Sb_2Se_3) measured using ultraviolet-visual spectroscopy (UV-Vis). The reflectance (R) and transmittance (T) is given as a percentage as a function of the wavelength of the light.

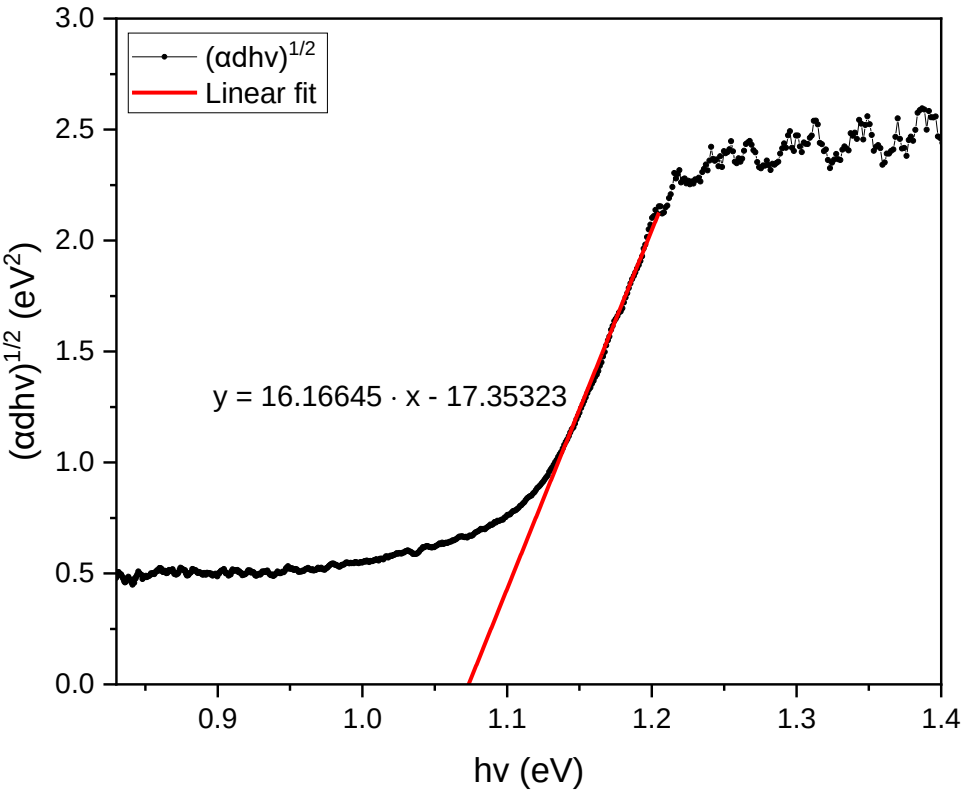

Figure 3: Linear fitting used to extract the indirect bandgap from the absorption coefficient of antimony selenide. The linear equation for the fitting is shown in the figure.

In Figure 3 the method described in section 3.2.1 for extracting the band gap from the UV-Vis data is applied. The figure shows the linear fit of the linear region of $(\alpha dh\nu)^{\gamma}$, with $\gamma = 1/2$ to find the indirect band gap. The linear fit has a slope of $a = 16.16645$ and an intercept of $b = -17.35323$. This gives us the linear equation

$$y = ax + b = 16.16645 \cdot x - 17.35323 \tag{33}$$

for the fitted curve. Using equation 21 we find from the linear equation that the indirect band gap of the antimony selenide film is

$$E_g = -\frac{b}{a} = \frac{17.35323}{16.16645} = 1.07341 \tag{34}$$

Thus, we have found that the indirect band gap of antimony selenide is approximately $E_g = 1.07\ eV$. Which is a bit higher than the 1.03 eV band gap reported in the literature (Chen et al., 2015).

Figure 4 is similar as Figure 3 only for the direct band gap case, with $\gamma = 2$ instead of $\gamma = 1/2$. From it we have the linear fit with a slope of $a = 529.58575$ and an intercept at $b = -617.08664$. This gives us the linear equation for the fitted curve

$$y = ax + b = 529.58575 \cdot x - 617.08664 \tag{35}$$

Again, applying the method described in section Ultraviolet-visual spectroscopy3.2.1 and using equation 21 we find from the linear equation that the indirect band gap of the antimony selenide film is

$$E_g = -\frac{b}{a} = \frac{617.08664}{529.58575} = 1.165225 \tag{36}$$

Thus, we have found that the direct band gap of antimony selenide is approximately $E_g = 1.17\ eV$. In this case, in contrast to the indirect band gap, we find the calculated band gap to agree very well, by being exactly equal, to the reported 1.17 eV (Chen et al., 2015).

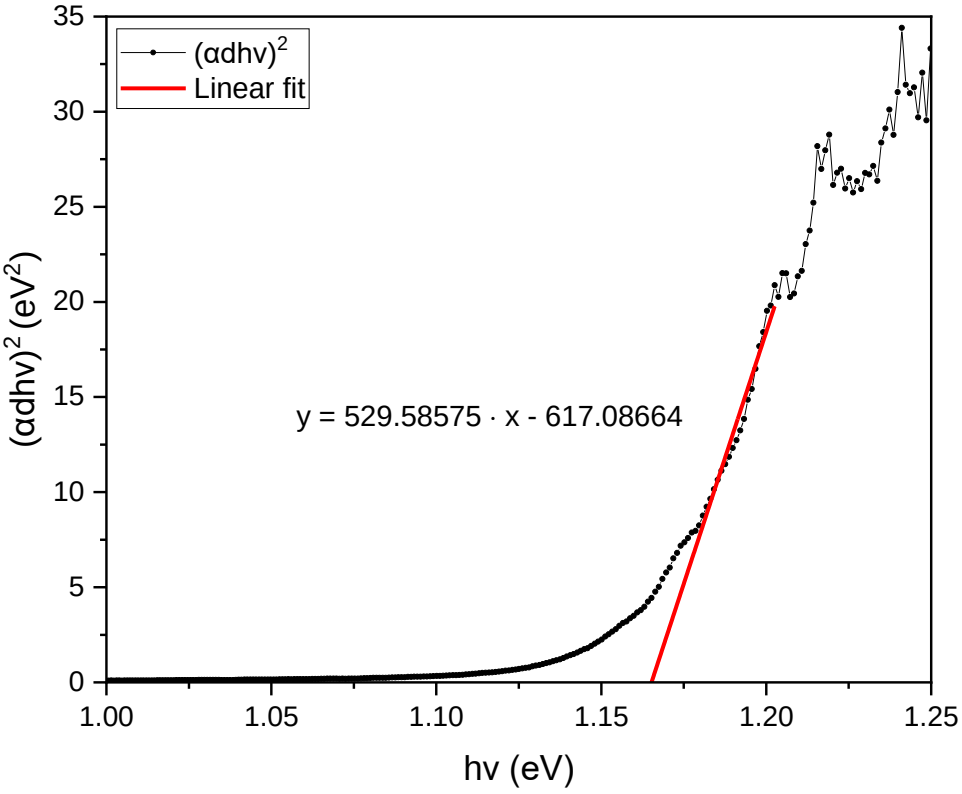

Figure 4: Linear fitting used to extract the direct bandgap from the absorption coefficient of antimony selenide. The linear equation for the fitting is shown in the figure.

4.2.2 P3HT

For P3HT the reflectance and transmittance measured for 1% P3HT using UV-Vis is given in Figure 5 below. Reflectance and transmittance were measured for both 0.5% and 1% P3HT deposited on glass in order to extract the band gap. However, only 1% P3HT gave results which were usable in the determination of band gap. The reason for why 0.5% P3HT did not give good results is most likely that the film is too thin to accurately measure transmittance and reflectance. Here we observe a steep increase in transmittance at about 600 nm. 600 nm corresponds to an energy of about 2.1 eV, which is close to the band gap of the material. A fall in the transmittance around the band gap is expected, as shorter wavelengths have higher energies which then will be absorbed. Interestingly the transmittance quickly increases again for shorter wavelengths. This appears to be an issue with the measurements as the transmittance increases above 100 %, and nothing related to the material. In contrast to antimony selenide,

we see that for P3HT the reflectance is high when the transmittance is low, and the other way around. For antimony selenide the transmittance and reflectance followed each other closely.

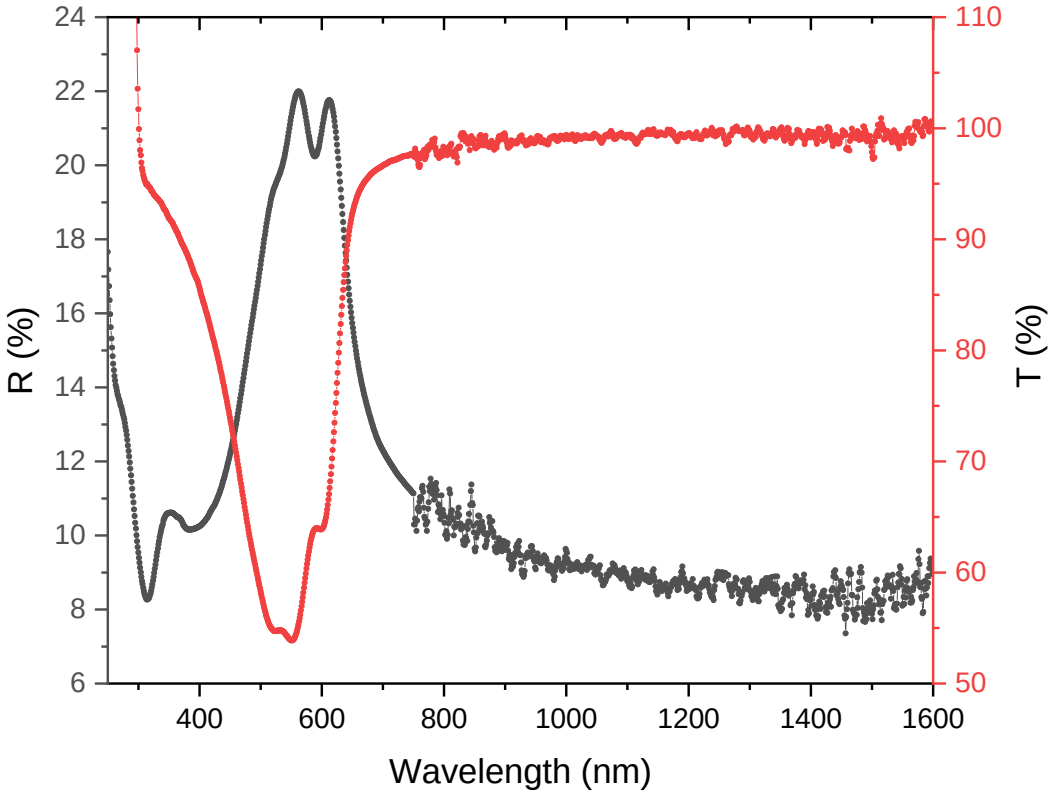

Figure 5: Reflectance and transmittance of 1% P3HT measured by UV-Vis.

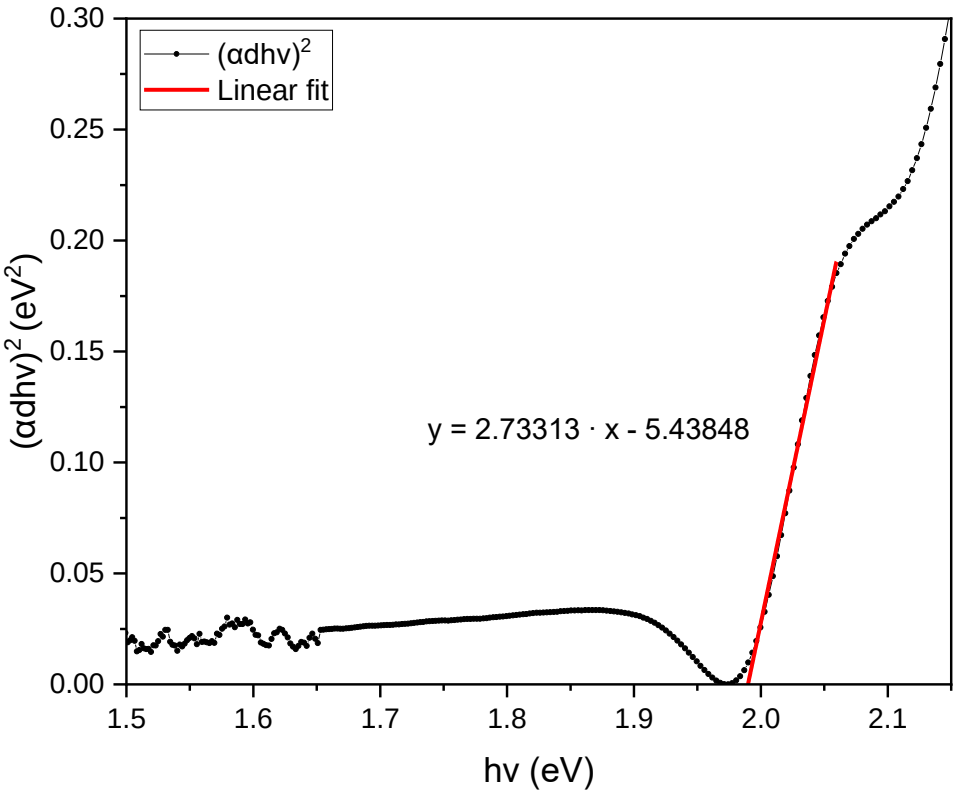

Figure 6: Linear fitting used to extract the direct bandgap from the absorption coefficient of P3HT. The equation for the linear fit is given in the figure.

Figure 6 shows $(\alpha dh\nu)^{\gamma}$, with $\gamma = 2$ to find the indirect band gap, plotted as a function of $h\nu$ together with the linear fit extended down to the x-axis. The equation of the linear fit is given in the figure. It has an intercept at $b = -5.43848$ and a slope of $a = 2.73313$. The band gap is then given by equation 21, we get

$$y = 0 \tag{37}$$

$$x = -\frac{b}{a} = \frac{5.43848}{2.73312} = 1.98984 \tag{38}$$

Thus, we have found that the band gap of P3HT is approximately $E_g = 1.99\ eV$. Compared to the 1.9 eV (Dadhich et al., 2021) band gap of P3HT reported in the literature, the band gap obtained here is a bit higher.

4.3 X-Ray Diffraction

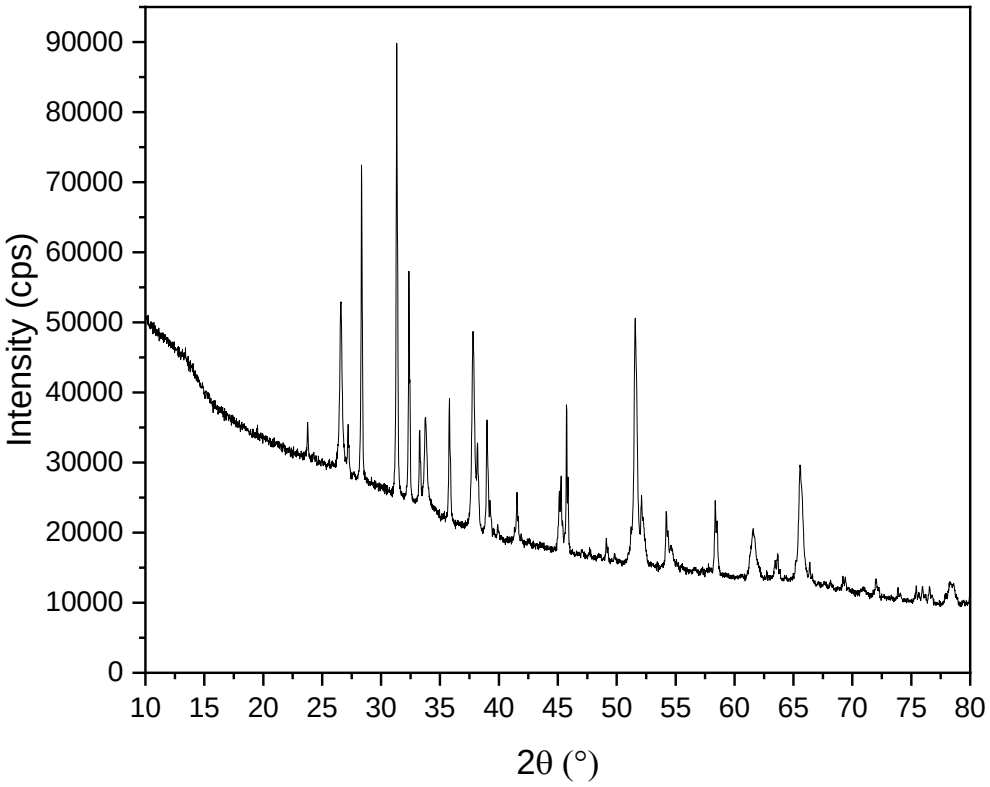

Figure 7: Raw XRD pattern for antimony selenide absorber layer

The raw unprocessed data from the x-ray diffraction (XRD) is shown in Figure 7. Figure 8 shows the main peaks of the data after subtraction of the baseline. The intensity of peaks is measured in counts per second (cps). 2θ corresponds to the angle between the incoming x-ray and the x-ray reflected from the crystal planes. As seen from Figure 7 no significant peaks occur before $2\theta = 23.78°$. From Figure 8 we see that the two peaks with the highest intensity occur at $2\theta = 28.34°$ and $2\theta = 31.32°$.

In section 2.3.2 the XRD conditions indicating desired orientation was given. They were a lack of peak around $2\theta = 17°$ for the (120) crystal plane and high intensity for the (211) peak at $2\theta = 28.4°$ and the (221) peak at $2\theta = 31.4°$ (Hutter et al., 2018). The results from the XRD measurements here showed a lack of peaks before $2\theta = 23.78°$, and, thus, no peak around $2\theta = 17°$ either, and the two strongest peaks at $2\theta = 28.34°$ and $2\theta = 31.32°$. This corresponds very well to these conditions, and indicates that by depositing antimony selenide

using the close space sublimation method with a seed layer described in section 3.1.3, the preferred crystal orientation with better charge transport properties was obtained.

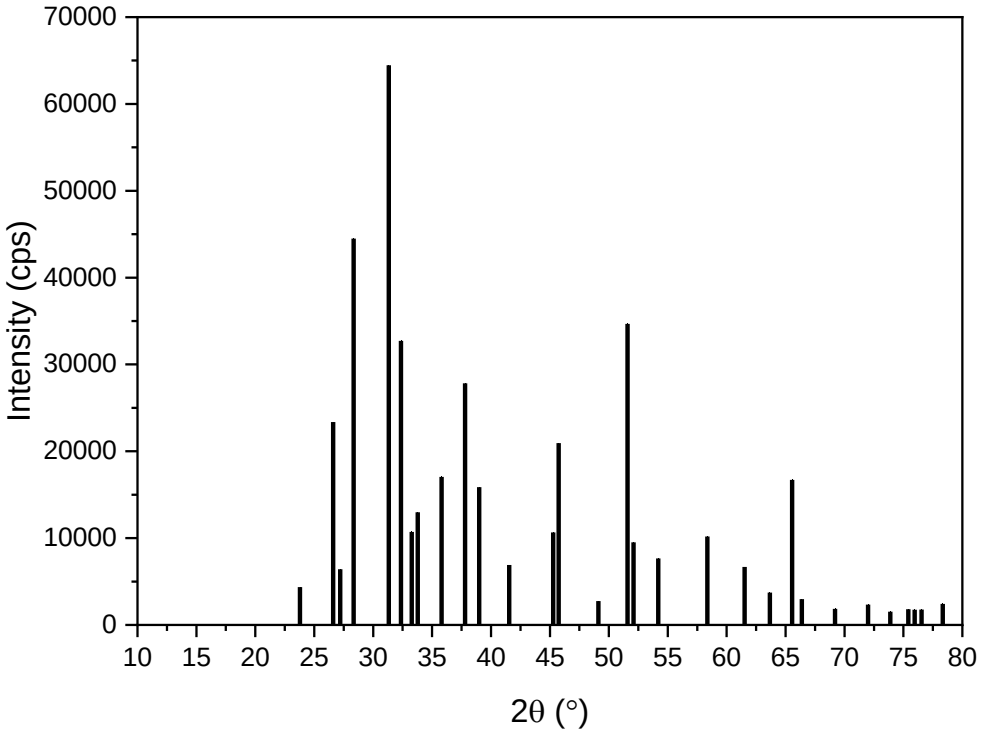

Figure 8: Peaks extracted from the XRD.

4.4 Hot probe measurements of antimony selenide absorber layer

Figure 9 shows the voltage between the cold and the hot probe as a function of time as the temperature of the hot probe is increased. For the two references, the n-type Bi_2S_3 exhibits an increasing positive voltage as the hot probe is heated. For the p-type SnS on the other hand we see the opposite trend with a decreasing negative voltage as the temperature of the hot probe increases. Antimony selenide exhibits a similar behaviour to SnS with a negative and decreasing voltage as the hot probe temperature increases. This observation indicates that antimony selenide is a p-type semiconductor.

After a period of time of heat applied, we see that the voltage built up between the probes, both for Bi_2S_3 and SnS, is much higher than what is achieved for Sb_2Se_3. This might be because of the low free carrier density in antimony selenide. With fewer free carriers, fewer carriers will

also diffuse away from the hot probe. There will be a smaller difference in charge between the two probes and thus also a smaller voltage.

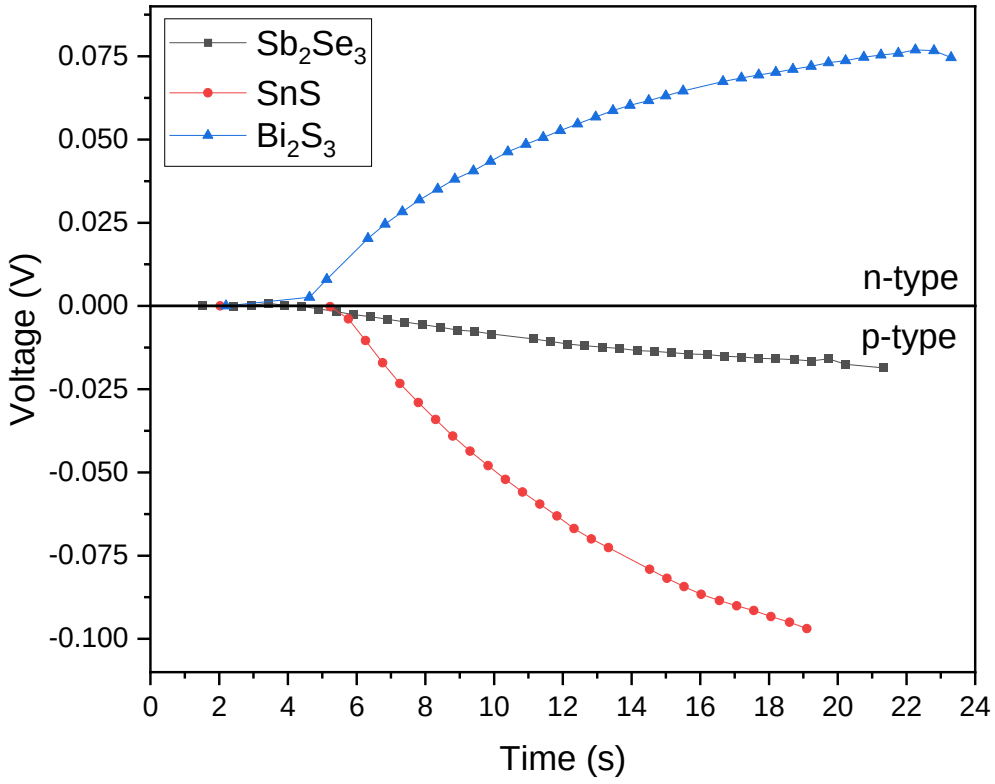

Figure 9: Hot probe measurements for determination of conductivity type. of antimony selenide. SnS and Bi_2S_3 given as a reference for p-type and n-type conductivity respectively. A positive voltage indicates n-type conductivity while a negative voltage indicates p-type conductivity.

4.5 Current voltage analysis and extraction of photovoltaic parameters of antimony selenide solar cell

The results from the J-V measurements are divided in two sections below. The first section considers the samples with a hole transport layer included, while the second section considers the bifacial solar cells. In both sections the references samples are included as well. In the two tables giving the results in the two following sections we have the parameters calculated from the J-V curve for the front and back side of each sample. These parameters are short circuit current density, open circuit voltage, maximum power, current density at maximum power point, voltage at maximum power point, fill factor and power conversion efficiency.

4.5.1 Antimony selenide solar cells with P3HT hole transport layer

Table 3 gives the results of the J-V measurements for the solar cells with hole transport layer and the references. The reference cell, named 14S_ref, is the standard monofacial cell without a hole transport layer. It has a power conversion efficiency of 4.81% when illuminated from the front side.

The 14S1 sample is identical to the reference cell, but with a 0.5% P3HT hole transport layer between the absorber and back contact. This sample shows a power conversion efficiency of 5.34% when illuminated from the front side. This is an increase of 0.53 percentage points compared to the reference cell, proving that the hole transport layer work as intended, that is it increases the efficiency of the solar cell. We can now take a look at the other parameters for these two devices to see what it is that causes this rise of efficiency. While the open circuit voltage remains more or less the same before and after the introduction of the hole transport layer, we see that the short circuit current density is improved. The goal of introducing the hole transport layer was to increase the collection of photogenerated carriers and reduce recombination at the back contact of the solar cell and thus increase the efficiency of the solar cell. From the results we see that this with the 14S1 sample this was caused solely by an improved current as the voltage remained more or less unchanged. Compared to the reference (14S_ref) the current increased from $27.97\ mA/cm^2$ for the sample without the hole transport layer, to $32.00\ mA/cm^2$ for the sample with the hole transport layer. Figure 10 shows the J-V and power curve of the reference and the sample with 0.5 % P3HT HTL. It is evident from the figure that the HTL improves the current from the solar cell.

A thicker 1% P3HT hole transport layer was used on the 13S1 sample. This sample has a reference with a higher efficiency, 13S_ref. Table 3 gives the results both for this sample, 13S1, and the reference which it must be compared to, 13S_ref. By comparing these cells, we can assess the effect of the 1% P3HT hole transport layer. The results show us that the thicker 1% P3HT hole transport layer does not cause any significant increase in the performance in comparison to the reference. Based on this we can conclude that the thinner 0.5% P3HT is a more suitable hole transport layer for antimony selenide based solar cells, than the thicker 1% P3HT.

Table 3: Results from J-V measurements for samples with hole transport layer and references. Short circuit current density (J_{sc}), open circuit voltage (V_{oc}), maximum power point power and current density and voltage, fill factor (FF) and power conversion efficiency (PCE) is calculated from the J-V data for both the front and back side for all the samples.

Sample name		**J_{SC} (mA/cm^2)**	**V_{OC} (mV)**	**P_{mpp} (mW/cm^2)**	**J_{mpp} (mA/cm^2)**	**V_{mpp} (mV)**	**FF (%)**	**PCE (%)**
13S_ref	Front	33.52	352.22	5.79	26.16	221.41	49.07	5.79
	Back	8.43	284.54	1.18	6.17	191.35	49.21	1.18
13S1	Front	23.33	348.94	3.96	17.89	221.41	48.68	3.96
	Back	5.34	283.58	0.79	4.15	191.35	52.39	0.79
13S1 (small contact)	Front	34.03	344.59	5.99	23.80	251.46	51.05	5.99
	Back	8.31	278.35	1.22	6.36	191.35	52.59	1.22
14S_ref	Front	27.97	345.91	4.81	21.72	221.41	49.70	4.81
	Back	6.15	284.39	0.94	4.90	191.35	53.55	0.94
14S1	Front	32.00	346.00	5.34	24.10	221.41	48.18	5.34
	Back	9.41	287.00	1.44	7.55	191.35	53.49	1.44

Table 4: Bifaciality factors for the solar cells with hole transport layer and the references calculated from the parameters extracted from the J-V curve given in Table 3.

Sample name	**J_{SC}**	**V_{OC}**	**P_{mpp}**	**J_{mpp}**	**V_{mpp}**	**FF**	**PCE**
13S_ref	25.15 %	80.79 %	20.38 %	23.59 %	86.42 %	100.29 %	20.38 %
13S1	22.89 %	81.27 %	19.95 %	23.20 %	86.42 %	107.62 %	19.95 %
13S1 (small contact)	24.42 %	80.78 %	20.37 %	26.72 %	76.10 %	103.02 %	20.37 %
14S_ref	21.99 %	82.22 %	19.54 %	22.56 %	86.42 %	107.75 %	19.54 %
14S1	29.41 %	82.95 %	26.97 %	31.33 %	86.42 %	111.02 %	26.97 %

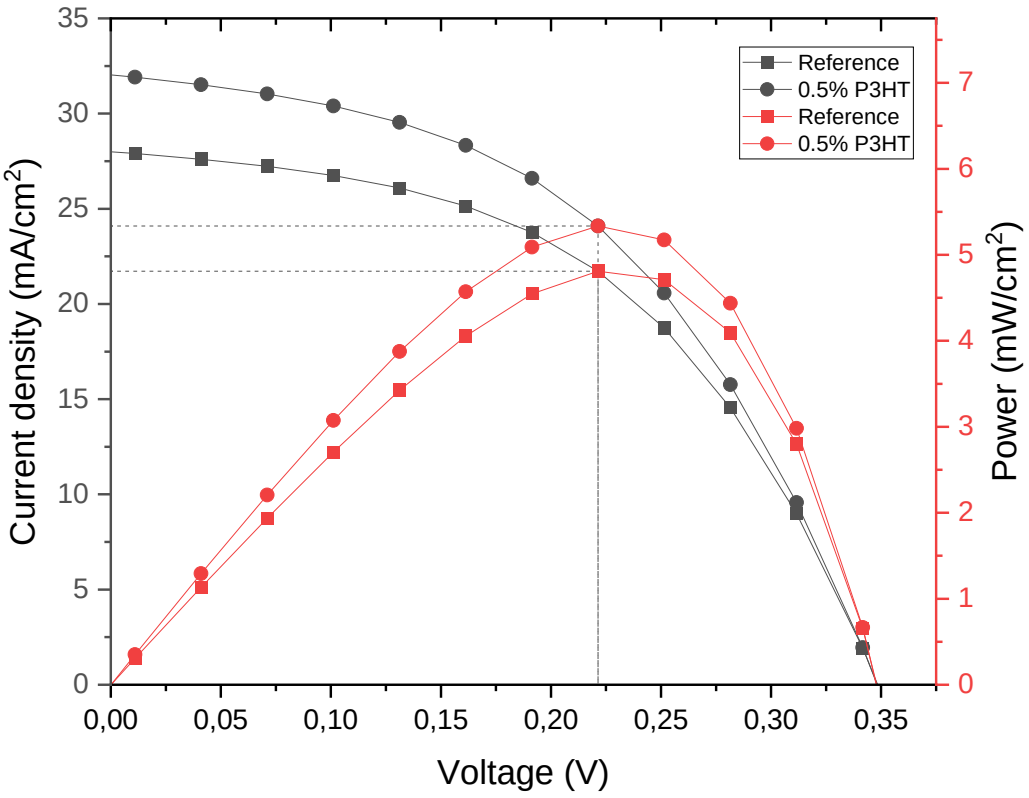

Figure 10: J-V and power – voltage characteristics for the 0.5% P3HT sample and the reference. The dashed lines marks the maximum power point. The current density and power is scaled so that the maximum power point coincides with the corresponding current density and voltage at MPP.

4.5.2 Bifacial antimony selenide solar cells

The results for the J-V measurements of the bifacial solar cells measured from the front side and the back side together with the reference is given in Table 5. 14S_ref is the reference for the bifacial cells. It is the reference despite not being bifacial because it allows us to compare the gains and losses in the bifacial samples compared to the standard monofacial solar cell. Among the bifacial solar cells, that is the cells with the ITO back contact, the 13L1 (small contact) sample achieved the highest power conversion efficiency. With a power conversion efficiency of 1.31% under front side illumination and 0.56% under back side illumination. These power conversion efficiencies are far from impressive. Thin film bifacial solar cells based on CdTe without hole transport layer and with ITO as back contact have achieved power conversion efficiencies of 7.0 % and 1.1 % for front and back side respectively (Pokhrel et al., 2022). While front side efficiency for this sample is higher than even the best monofacial

efficiencies achieved in this thesis, the back side efficiency is only about twice that of the antimony selenide sample.

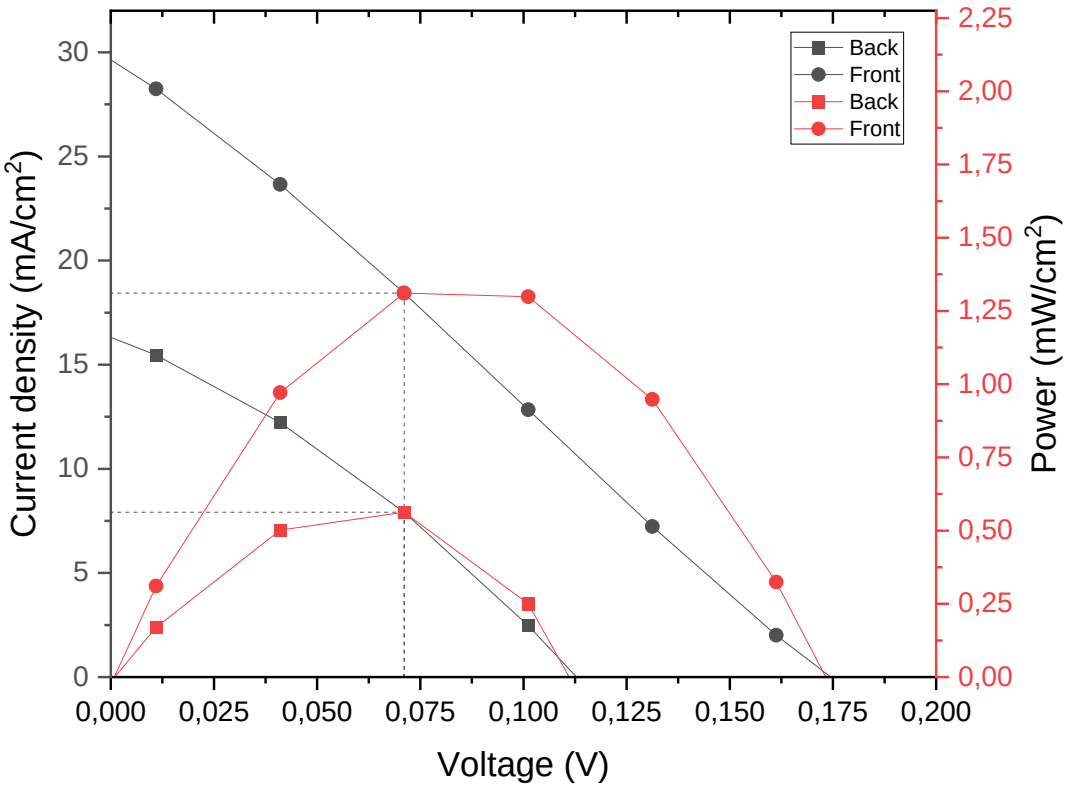

Figure 11: J-V and power – voltage characteristics for the best bifacial sample.

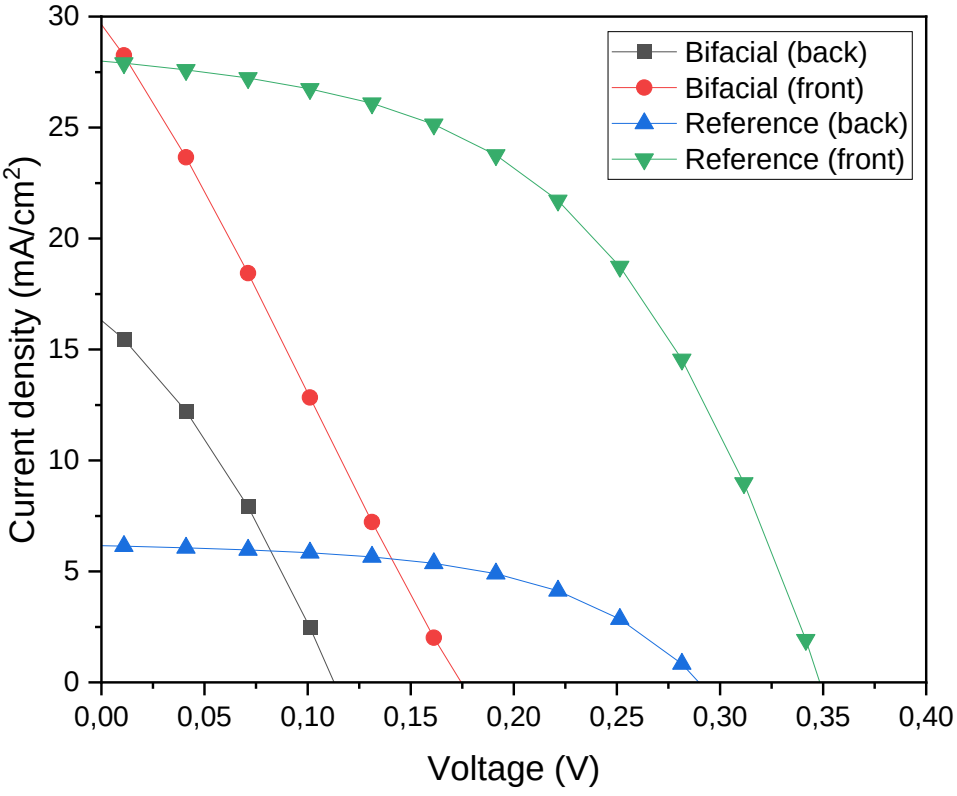

Figure 12: J-V curves for the best bifacial cell and the reference, under both front and back side illumination.

We see a large loss of efficiency compared to the reference cell for the bifacial cells, despite this there are still a few findings to note. For the monofacial cells the back contact is not transparent, and any light causing generation of carriers likely enters the absorber from the sides of the solar cell. The large decrease in short circuit current density and current density at maximum power point from the back side compared to the front side as seen in Table 3 was because of this expected. It is very limited how much light can enter through the side of the solar cells, compared to how much can enter through a transparent contact. When making the back contact transparent, and thus achieving bifaciality, we also expect a larger current to come from the backside of the solar cell. We observe this for the 13L1 (small contact) sample which exhibits a higher short circuit current density than the reference. For the front side this short circuit current density is only barely higher, but under rear side illumination this sample delivers more than twice the short current density of the reference. Hence, it is clear that the current is not the issue for the efficiency of the bifacial solar cells, and we also see that we achieved the expected result of increasing the current delivered when illuminated from the back side.

Considering the open circuit voltage, we see that the bifacial 13L1 (small contact) sample only has about half the voltage of the reference from the front side, and for the back side there is an even larger deficiency. It, thus, appears that the ITO back contact works very well at collecting the charge carriers, but struggles a lot with the voltage with a large loss compared to the reference. Figure 11 shows the J-V and power curves for the best bifacial sample. In Figure 12 the J-V curve of the reference and the best bifacial cell is given for both the back side and the front side. It is clear from the figure how the transparent back contact improved the current from the back side, while we see the large loss of open circuit voltage from both the front and back side.

Another observation is that the large fall in current density from short circuit to maximum power point, and the large fall in voltage from open circuit the maximum power point also contributes much to the low efficiency. While the reference had a 22.35% and 35.99% change in current density and voltage respectively, the highest efficiency bifacial cell had a 36.98% and 59.79% change equivalently. This is evident from the fill factor as well, with the reference having a fill factor of 49.7% while the bifacial have a fill factor of only 25.33%. Naturally, as the power conversion efficiency of solar cells is a function of the fill factor, as seen in equation 5, this translates to a lower power conversion efficiency for the bifacial cell than the reference cell.

But why is the current lower from the back side than from the front side? One explanation is of course the lack of transparency of the back contact, and we have seen that increasing the transparency of the back contact does indeed increase the current. But as detailed in section 2.2.3 of the theory section, a smaller current is expected from the back side because the electron hole pairs are generated further away from the p-n junction when illuminated from the back side than for front side illumination. This increases the chance of the electron hole pairs recombining before being separated by the electric field in the p-n junction.

The bifaciality factors for the monofacial and bifacial solar cells are given in Table 4 and Table 6 respectively. The bifaciality factors are calculated for all of the parameters in Table 3 and Table 5. With bifaciality factors, which is just the fraction of the rear side parameter to the front

side parameter given in percentage, it is easy to compare how the solar cell performs under front and rear side illumination. For the bifaciality factor the higher the percentage is to a hundred the better it is, with a hundred percentage indication an equal performance at the front and back side. From Table 4 and Table 6 we see that the bifaciality factor is under 100% for short circuit current density, open circuit voltage, maximum power point power, maximum power point current density, maximum power point voltage and power conversion efficiency for all samples. This tells us that these parameters have a higher value for the front side than the back side, as expected. The only exception from this is the fill factor. In fact, we see from Table 4 and Table 6 that for all samples the fill factor is better for the rear of the solar cell than for the front. Once more, we can compare the monofacial cells to the bifacial ones. The bifacial cells all exhibit higher bifaciality factors for short circuit current, power at mpp, current density at mpp, fill factor and power conversion efficiency (except for the 14L1 sample). For open circuit voltage the monofacial cells actually exhibits the highest bifaciality factors, and this is also the same for the voltage at mpp, except that the 13L1 (small contact) sample gives a 100%. As a result, it gives exactly the same voltage at mpp. The fact that it is precisely the same is explained by the measurements being discrete. When extracting the voltage corresponding to the maximum power point the accuracy is limited because the voltage is only measured at certain points, and without making any fittings of the data, only these discrete points can be used. This stands in contrast to the method used when extracting open circuit voltage and short circuit current. In those cases, the four measurements closest to the axis were used to make a linear fit and from that calculate the short circuit current or open circuit voltage.

The effects that shunt resistance (Rsh) have on the performance of solar cells is that with decreasing shunt resistance we also get reducing open circuit voltage and fill factor (Mavlonov et al., 2020). Looking back at the results in Table 5 we see that the best performing bifacial cell has $V_{oc} = 176.84$ mV and $FF = 25.33$ % for the front side and $V_{oc} = 111.07$ mV and $FF = 31.82$ % for the back side. In comparison the reference cell has $V_{oc} = 345.91$ mV and $FF = 49.70$ % for the front side and $V_{oc} = 284.39$ mV and $FF = 53.55$ % for the back side. We observe a large loss in both open circuit voltage and fill factor when going from the monofacial to the bifacial design. This might be explained by a lower shunt resistance in the bifacial than the monofacial cell.

Table 5: Results from J-V measurements for the bifacial solar cells and the reference. Short circuit current density (J_{sc}), open circuit voltage (V_{oc}), maximum power point power and current density and voltage, fill factor (FF) and power conversion efficiency (PCE) is calculated from the J-V data for both the front and back side for all the samples.

Sample name		**J_{SC} (mA/ cm^2)**	**V_{OC} (mV)**	**P_{mpp} (mW/ cm^2)**	**J_{mpp} (mA/ cm^2)**	**V_{mpp} (mV)**	**FF (%)**	**PCE (%)**
14S_ref	Front	27.97	345.91	4.81	21.72	221.41	49.70	4.81
	Back	6.15	284.39	0.94	4.90	191.35	53.55	0.94
13L1 (small contact)	Front	29.26	176.84	1.31	18.44	71.11	25.33	1.31
	Back	15.92	111.07	0.56	7.91	71.11	31.82	0.56
13L1	Front	15.16	114.67	0.45	6.27	71.11	25.64	0.45
	Back	6.85	70.41	0.15	3.58	41.05	30.45	0.15
13S (bifacial)	Front	4.57	216.56	0.15	2.05	71.11	14.76	0.15
	Back	3.40	99.93	0.08	1.82	41.05	22.00	0.08
14L1	Front	15.13	271.41	0.79	7.76	101.17	19.13	0.79
	Back	4.41	98.54	0.13	3.14	41.05	29.66	0.13

Table 6: Bifaciality factors for the bifacial solar cells and the reference calculated from the parameters extracted from the J-V curve given in Table 5.

Sample name	**J_{SC}**	**V_{OC}**	**P_{mpp}**	**J_{mpp}**	**V_{mpp}**	**FF**	**PCE**
14S_ref	21,99 %	82,22 %	19,54 %	22,56 %	86,42 %	107,75 %	19,54 %
13L1 (small contact)	54,41 %	62,81 %	42,75 %	42,90 %	100,00 %	125,62 %	42,75 %
13L1	45,19 %	61,40 %	33,33 %	57,10 %	57,73 %	118,76 %	33,33 %
13S (bifacial)	74,40 %	46,14 %	53,33 %	88,78 %	57,73 %	149,05 %	53,33 %
14L1	29,15 %	36,31 %	16,46 %	40,46 %	40,58 %	155,04 %	16,46 %

Looking back at Table 4, another interesting result is seen for the 14S1 sample. This sample exhibits increased bifaciality factors for short circuit current density, maximum power, current density at maximum power point, and the power conversion efficiency. Despite not any of these cells being bifacial, in that the back contact is of gold, this still shows us that the 0.5% P3HT hole transport layer might be useful to improve the performance from the backside for bifacial solar cells. The use of a hole transport layer has been shown to greatly improve the efficiency of CdS based bifacial solar cells (Pokhrel et al., 2022). The effect on the P3HT hole transport layer on the efficiency of the bifacial solar cell is investigated in the modelling part of the thesis.

4.6 External quantum efficiency analysis Sb2Se3 solar cells

The table below gives the short circuit current density (J_{sc}) from the J-V curves (see the J-V section and the tables there) and the short circuit current density obtained by integrating the external quantum efficiency (EQE) curve using equation 8 as explained in the EQE theory section.

Ideally, the short circuit current density calculated from the two measurement methods, J-V measurements and EQE, should be equal, but as we can see from the results in Table 7 it is not in most cases. The difference is calculated as short circuit current density from J-V minus the short circuit current density from external quantum efficiency. The percentage change is calculated by dividing the difference by the short circuit current density from the J-V curves. A negative difference tells us that the short circuit current density is higher from EQE while a positive means that it is smaller. For the percentage change a negative percentage means that we have an increase, while a positive percentage means that we have a decrease.

Table 7: Short circuit current density (J_{sc}) calculated from J-V curve measurements, second column, and from integration of external quantum efficiency measurements, third column. Column four gives the difference between the two measures and column five gives the percentage change from column two to column three.

Sample name		JSC from J-V [mA/cm2]	JSC from EQE [mA/cm2]	Difference [mA/cm2]	% change from J-V to EQE
13L1	Front	15,16	24,78	-9,62	-63,46%
	Back	6,85	2,35	4,5	65,69%
13S (bifacial)	Front	4,57	9,37	-4,8	-105,03%
14L1	Front	15,13	25,67	-10,54	-69,66%
	Back	4,41	2,26	2,15	48,75%
13S_ref	Front	33,52	27,87	5,65	16,86%
	Back	8,43	0,75	7,68	91,10%
13S1	Front	23,33	23,05	0,28	1,20%
	Back	5,34	0,32	5,02	94,01%
14S_ref	Front	27,97	25,64	2,33	8,33%
	Back	6,15	2,72	3,43	55,77%
14S1	Front	32,00	30,97	1,03	3,22%
	Back	9,41	0,81	8,6	91,39%

Considering the results in Table 7 we see very varying degrees of correspondence between the short circuit current density calculated from J-V measurements and from integration of external quantum efficiency. While the lowest percentage difference between the two is only 1.2%, which is a very good correspondence, the highest percentage difference is an increase of 105,03%, meaning that the short circuit current from the EQE was more than double that from the J-V curves. While it is the 13S1 sample that sees the smallest change for the front side, it is the 14S_ref sample that see the smallest change for the backside. However, for the backside

this is still very much higher at 55.77%. One interesting observation is that for all the bifacial cells we see an increase for the front side short circuit current, while it is for the front side of the monofacial cells that we see the smallest changes, and in this case these changes are decreases. It appears as the changes are smaller at higher current densities, as we see for the monofacial cells, which have relatively good agreement for all the front side, while it gets worse for the back side, which all also have very much lower current densities. For the bifacial cells, however, we see a high disagreement for both the front and back sides.

What can the causes of the differences in the short circuit current density from J-V curves and EQE be? One possibility is differences in the measurement setup. While for the J-V curves a solar simulator with temperature control and a closed compartment was used, for the EQE measurements no temperature control was used, and the sample was not as well protected from other light sources (but probably well enough). Another potential source of the difference is the light source used for the two measurements. It is possible that differences in the spectra from the light sources also cause differences in the calculated short circuit current density. The EQE was calibrated using a well performing sample. The better agreement for samples with high efficiency might indicate that the calibration is not suitable for devices with lower current densities.

Figure 13 below shows the external quantum efficiency plotted together with the short circuit current density integrated from the external quantum efficiency. As we can see from the figure the slope of the integrated current depends on the value of the EQE. The lower the EQE value, the flatter the slope of the current. At the start of the graph at 300 nm we see that as the EQE increases so does the slope of the current. It increases until the peak EQE value is reached at around 400 nm, and from here the slope of the current gets less and less steep as the EQE declines, and it reaches a plateau when the EQE goes to zero. The interpretation of the integrated current density curve is that for each wavelength the current density for that specific wavelength is added to the total. So that when we read the value at a specific wavelength, what we get is the sum of the current density contribution from every wavelength from 300 nm and up to and including the wavelength that we look at the value for.

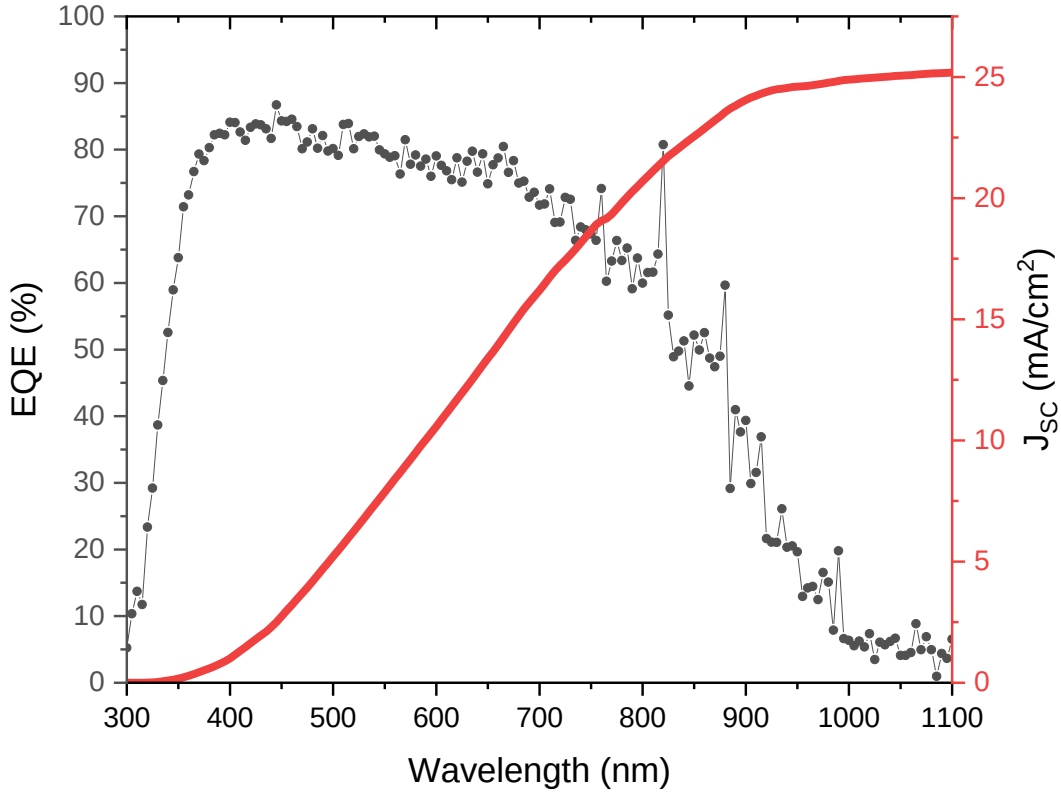

Figure 13: External quantum efficiency (EQE) as a function of wavelength for the 14S_ref sample. Together with the EQE we have the integrated EQE which gives the short circuit current density when integrated over the entire wavelength range.

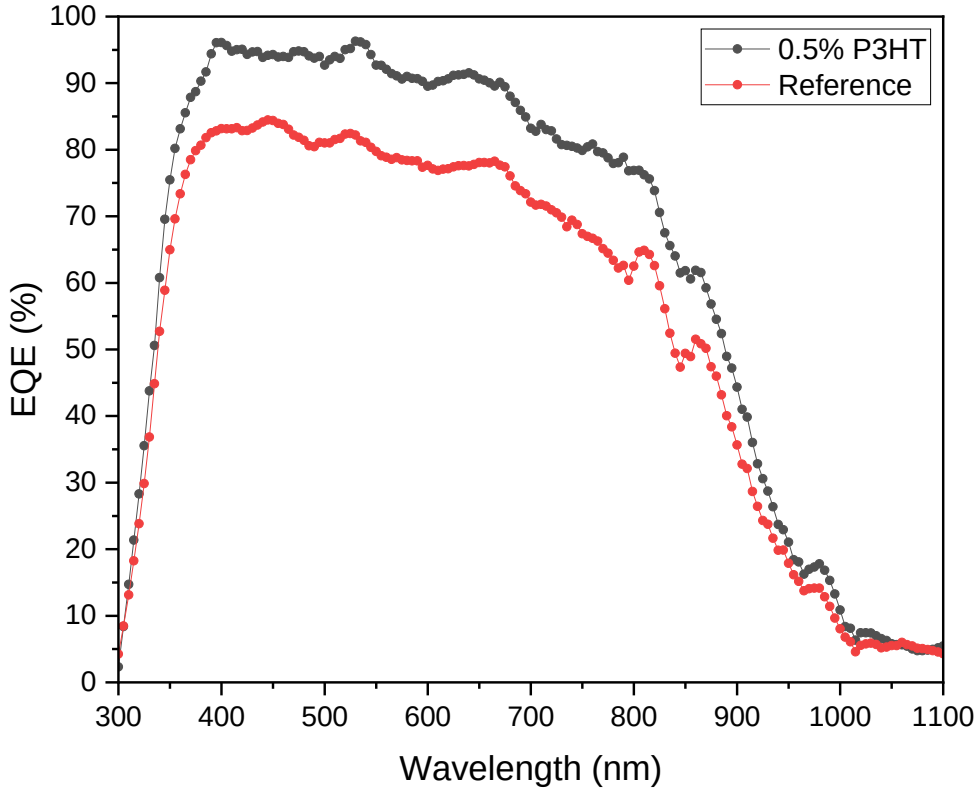

Figure 14: External quantum efficiency (EQE) of the sample with 0.5% P3HT hole transport layer and the reference sample. The plot shows how the EQE was improved after implementation of the 0.5% P3HT hole transport layer.

Figure 14 shows the external quantum efficiency of the solar cell with the 0.5% P3HT hole transport layer and the reference solar cell. We can see from the graph that the hole transport layer does enhance the current of the solar cell. It over improves the current of the solar cell, but the improvement is highest in for the wavelengths where the EQE was best for the reference. The improvement for the wavelengths where the reference is struggling is small. This seems reasonable as the low EQE at certain wavelengths is likely due to properties of the absorber, such as lower absorption of wavelengths with energies very close to the band gap, and not something the hole transport layer can affect.

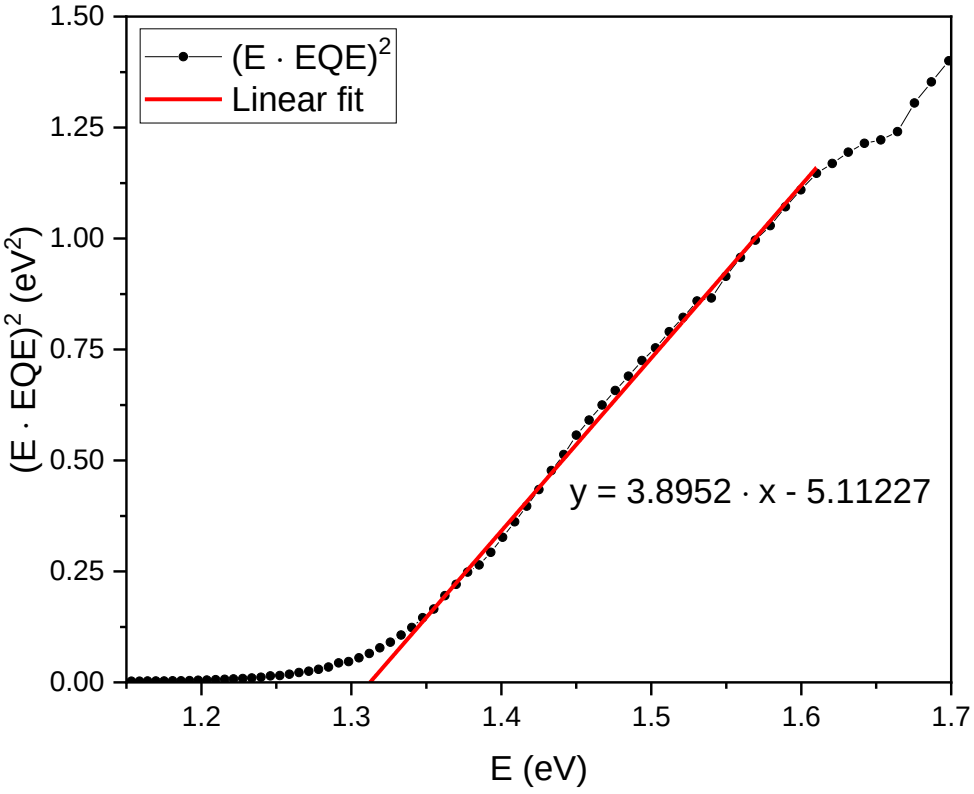

Figure 15:Band gap extracted from EQE for the reference sample

Utilising the method explained in section 3.2.5 the band gap of the antimony selenide absorber is obtained from the measured external quantum efficiency. Figure 15 and Figure 16 shows the resulting plot of $(E \cdot EQE)^2$ as a function of E and the linear fit used to extract the band gap. Applying … we get

$$E_g = \frac{5.11227}{3.8952} = 1.3125 \tag{38}$$

for the reference, and

$$E_g = \frac{7.5137}{5.7327} = 1.3107 \tag{39}$$

for the sample with 0.5% P3HT HTL. Thus, for both samples we obtain a consistent results with a bandgap of approximately 1.31 eV. Comparing to the 1.17 eV direct band gap obtained from UV-Vis measurements, which was equal to the direct band gap reported in the literature (Chen et al., 2015), we here observe a much higher band gap.. This might be an indication of the method not being robust enough and giving inaccurate results. However, as the band gap

here is from the solar cell, while in UV-Vis the absorber is deposited directly on roughened glass, the different substrates might affect the band gap (Carron et al., 2019). A band gap of 1.25 eV was obtained using the same EQE method (Krautmann et al., 2021), which is much closer to the value obtained here.

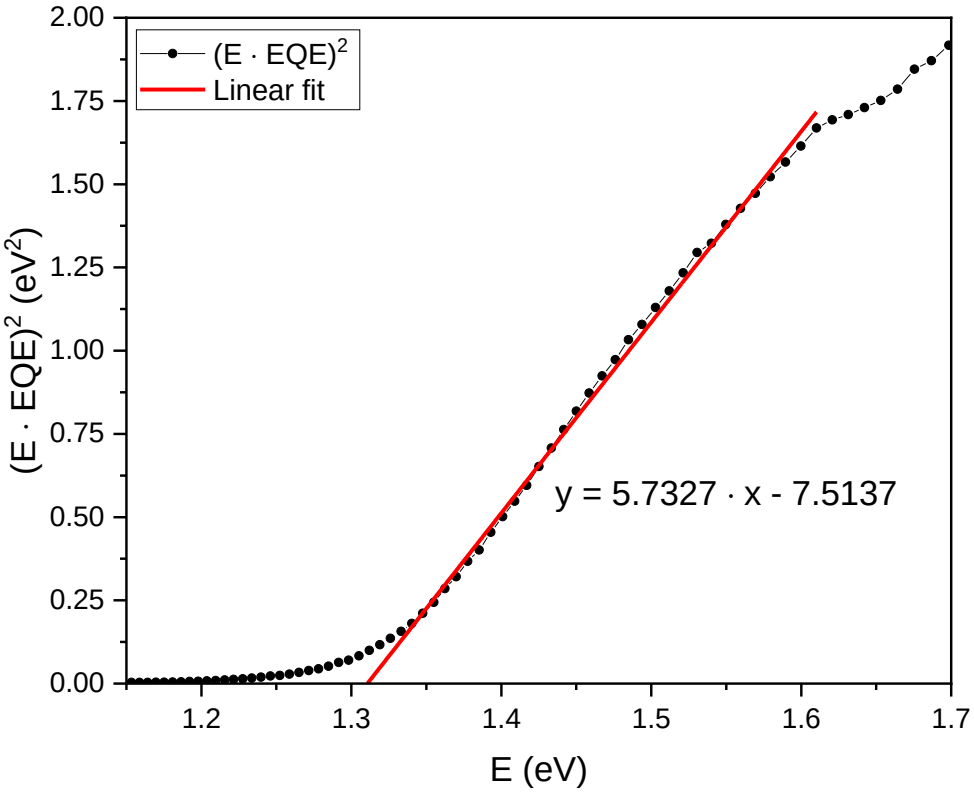

Figure 16: Band gap extracted from EQE for sample with 0.5% P3HT

4.7 Modelling of Sb2Se3 solar cells

This section gives and discusses the results from the modelling. The results and discussion are presented in the same order as the modelling was described in section 3.3

4.7.1 Analysis of parameters of the monofacial antimony selenide based solar cells

The first step was to optimise the thickness of the antimony selenide absorber. Figure 17 shows the result of the optimisation of the thickness of the antimony selenide. A peak efficiency of 15.21 % is achieved for an absorber thickness of 0.7 μm. Decreasing or increasing the thickness from here degrades the performance of the solar cell. The efficiency falls below ten percent both when decreasing the thickness of the absorber to 0.1 μm and when increasing the thickness to 3 μm. This is consistent with the discussion in section 2.4 on the recombination in the absorber. The obtained optimal thickness is much lower than the diffusion length of 1.7 μm (Chen et al., 2017).

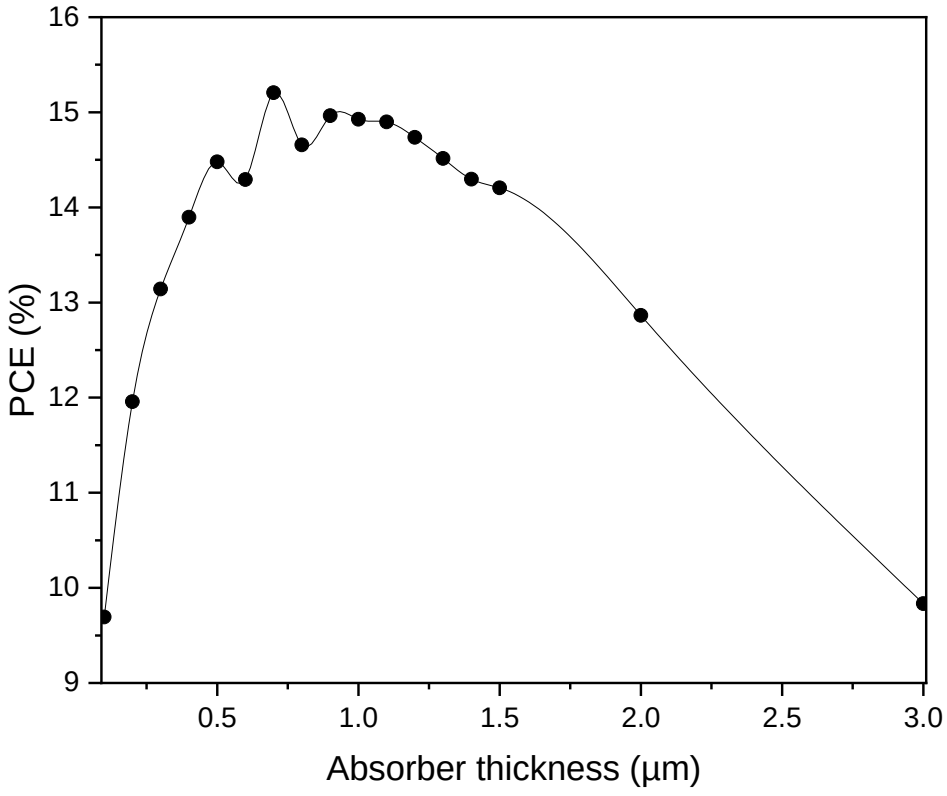

Figure 17: Power conversion efficiency as a function of absorber thickness.

After the optimal thickness of 0.7 μm was found, this thickness was used when investigating the effect of doping on the power conversion efficiency. Figure 18 shows how the power conversion efficiency depends on the absorber doping density. The doping concentration, of acceptors, resulting in the highest efficiency of 15.52 % was 2.154×10^{15} cm^{-3}. However, despite the very large differences in acceptor concentration, the change in power conversion efficiency is relatively small. From the lowest efficiency of 15.20 % at 10^{12} cm^{-3} there is only an increase of 0.32 percentage points to the highest efficiency at 2.154×10^{15} cm^{-3}. Furthermore, a decrease in power conversion efficiency is observed when increasing the acceptor doping concentration above 2.154×10^{15} cm^{-3}. The highest efficiency was expected to be achieved for the highest doping density of 10^{16} cm^{-3} which is said to be the optimal doping density for the absorber (Chen et al., 2017). Still, we see that increasing the free carrier density from the 1.8×10^{13} cm^{-3} free carrier density of the antimony selenide is beneficial for the solar cell efficiency.

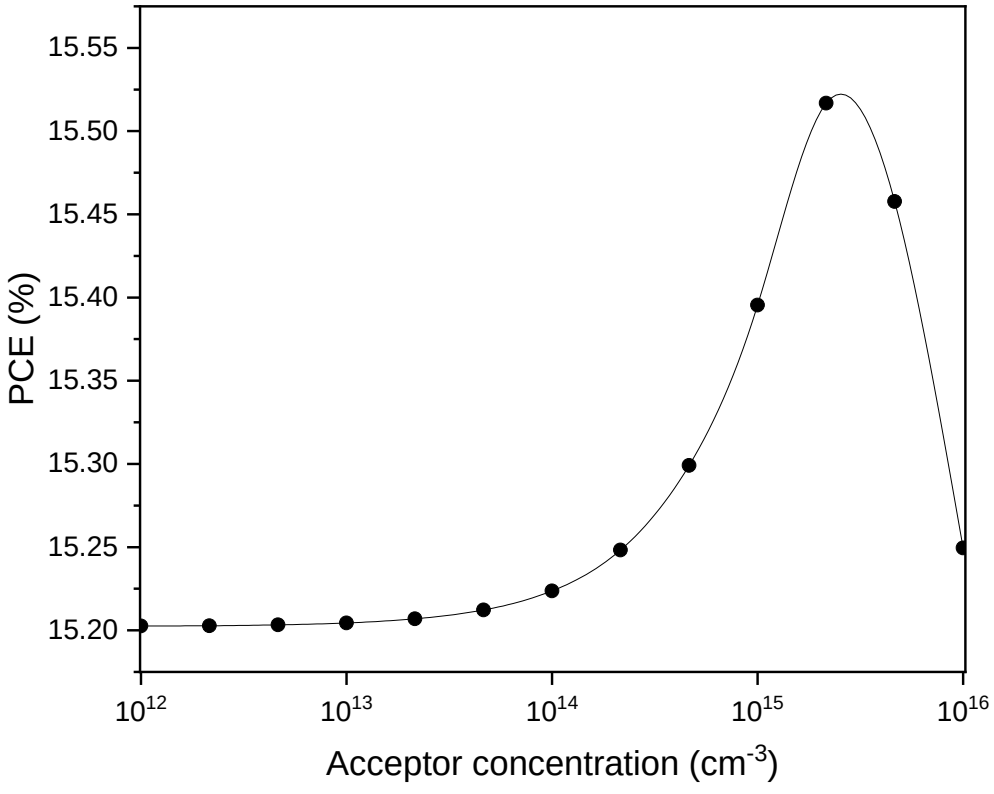

Figure 18: Power conversion efficiency as a function of acceptor concentration in the solar cell absorber.

However, a much larger gain in efficiency was expected from the doping of the absorber. It was based on this investigated if the optimal thickness of the absorber would be different with a doping density of 10^{16} cm^{-3}. It was investigated if this was related to the thickness of the absorber or not. As it is said in the literature that 10^{16} cm^{-3} is the optimal density of doping (Chen et al., 2017), this concentration was used when varying the thickness. Figure 19 confirms that with a higher doping concentration, a thicker absorber film results in a higher power conversion efficiency. In comparison to Figure 18 where the thickness of the absorber was optimised for the intrinsic free carrier density of antimony selenide, the efficiency does not fall off substantially with the increasing thickness. The peak efficiency of 17.36 % was found for a film thickness of 4 μm. For even thicker films the efficiency decreases, however, very slowly. While increasing the doping density but keeping the thickness constant at 0.7 μm only resulted in a minimal increment of the efficiency, doping the sample to 10^{16} cm^{-3} and increasing the thickness to 4 μm resulted in a 2.15 percentage points increase.

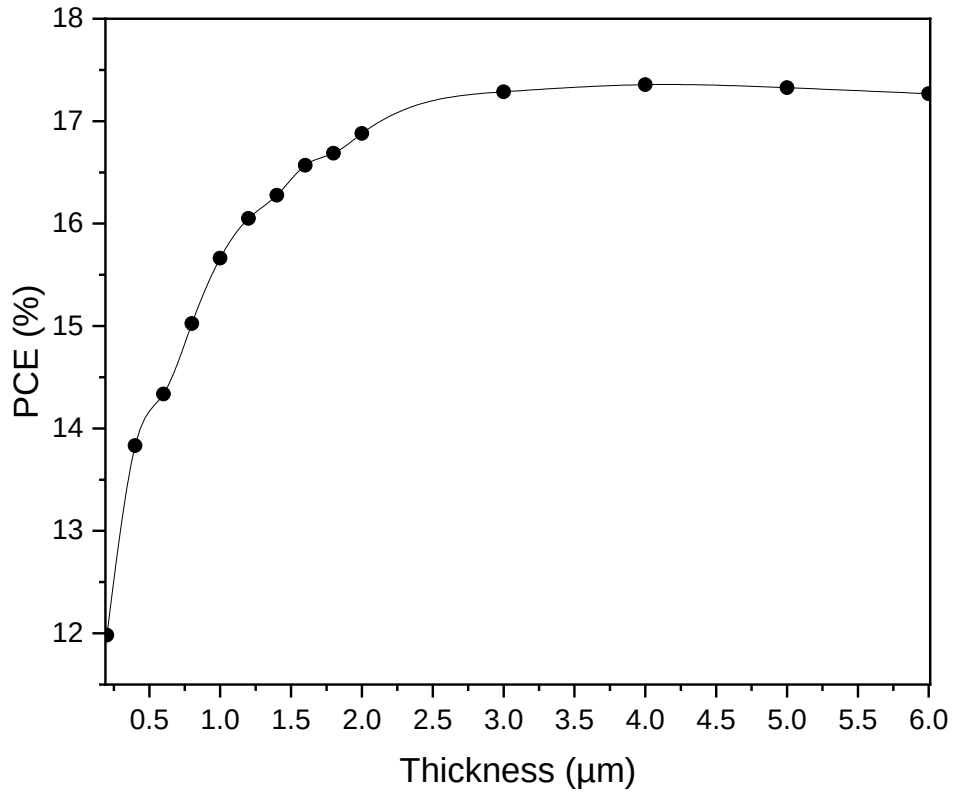

Figure 19:Power conversion efficiency as a function of thickness at 10^{16} cm^{-3} acceptor concentration.

Due to the large differences in the reported free carrier concentration of CdS, the sensitivity of the efficiency on the doping level of the absorber was analysed. Figure 20 shows how the power conversion efficiency depends on the free carrier concentration of the buffer layer. Compared to the 10^{18} cm^{-3} doping concentration used for the buffer for all the other simulations, a decrease in power conversion efficiency is observed for all lower densities. An increasing in the doping density, on the other hand, also gave an increase of the power conversion efficiency. It appears that for the constant thickness, the efficiency is more sensitive on the doping of the buffer than the absorber. This illustrates the importance of obtaining buffer films with high free carrier density. Using a film with a density of 10^{12} cm^{-3} instead of 10^{18} cm^{-3} lowers the power conversion efficiency from 15.21 % to 14.27 %.

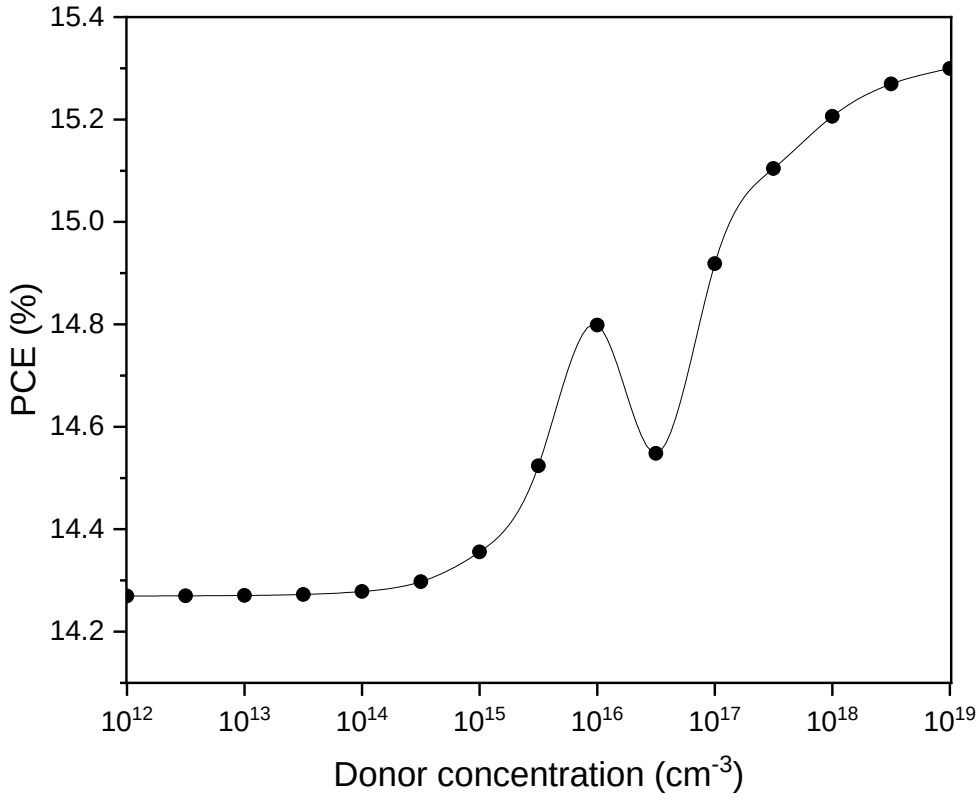

Figure 20: Power conversion efficiency as a function of the donor concentration in the buffer of the solar cell

The final parameter analysed for the monofacial cell is how the solar cell power conversion efficiency depends on the electron and hole lifetime. The results are shown in figure Figure 21. The electron and hole lifetime determines the recombination in the solar cell. The figure illustrates how important it is with a high carrier lifetime in order for the solar cell to perform well. For the lowest lifetimes simulated the efficiency is very dependent on it, while after about the lifetime of 10^{-7} s the curve flattens, and the efficiency is much less dependent on the increasing lifetime. From a lifetime of 10^{-9} s to a lifetime of 10^{-8} s the efficiency increases from 4.38 % to 11.82 %, while between 10^{-6} s to 10^{-5} s in comparison only a small increase from 16.26 % to 16.35 % is obtained.

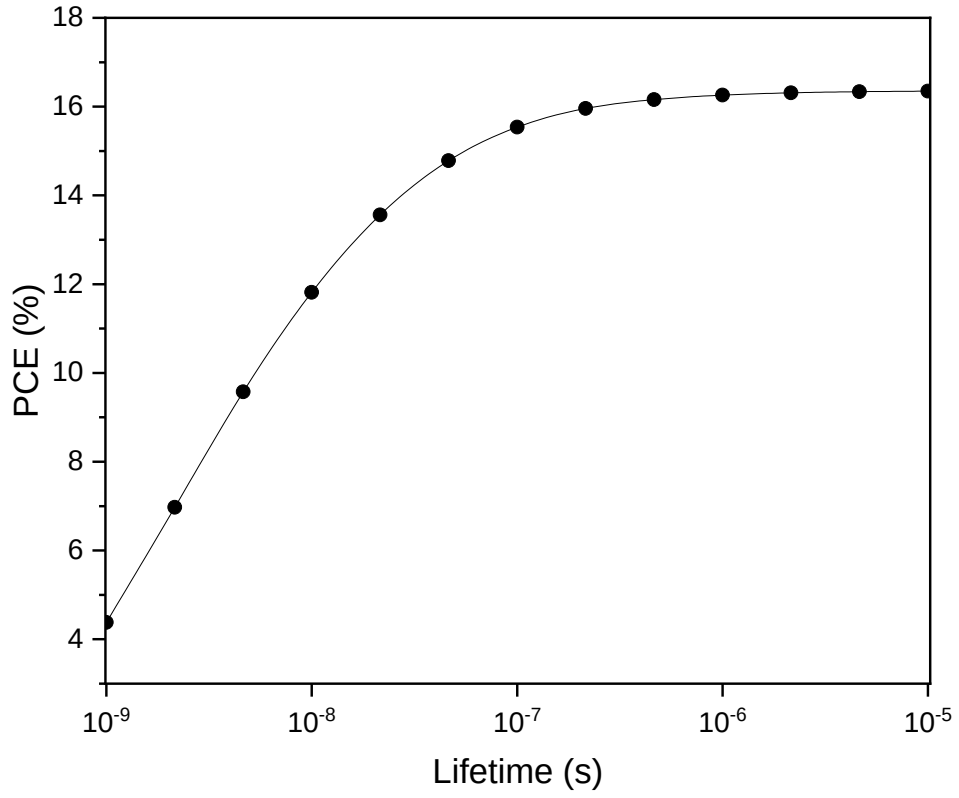

Figure 21: Power conversion efficiency as a function of electron and hole lifetime.

It is very beneficial to obtain lifetimes in the order 10^{-7} s or 10^{-6} s, but improving the lifetime beyond this does not result in large gains in efficiency. With the electron lifetime of 6.7×10^{-8} s, which the electron lifetime is assumed to be equal to for these simulations, antimony selenide could benefit from an increased lifetime.

4.7.2 Hole transport layer

The next step of the modelling was to implement the P3HT hole transport layer. When implementing it, the effect of its thickness was analysed. Figure 22 shows the efficiency of the solar cells with a P3HT hole transport layer implemented, and how the efficiency varies depending on the thickness of this hole transport layer.

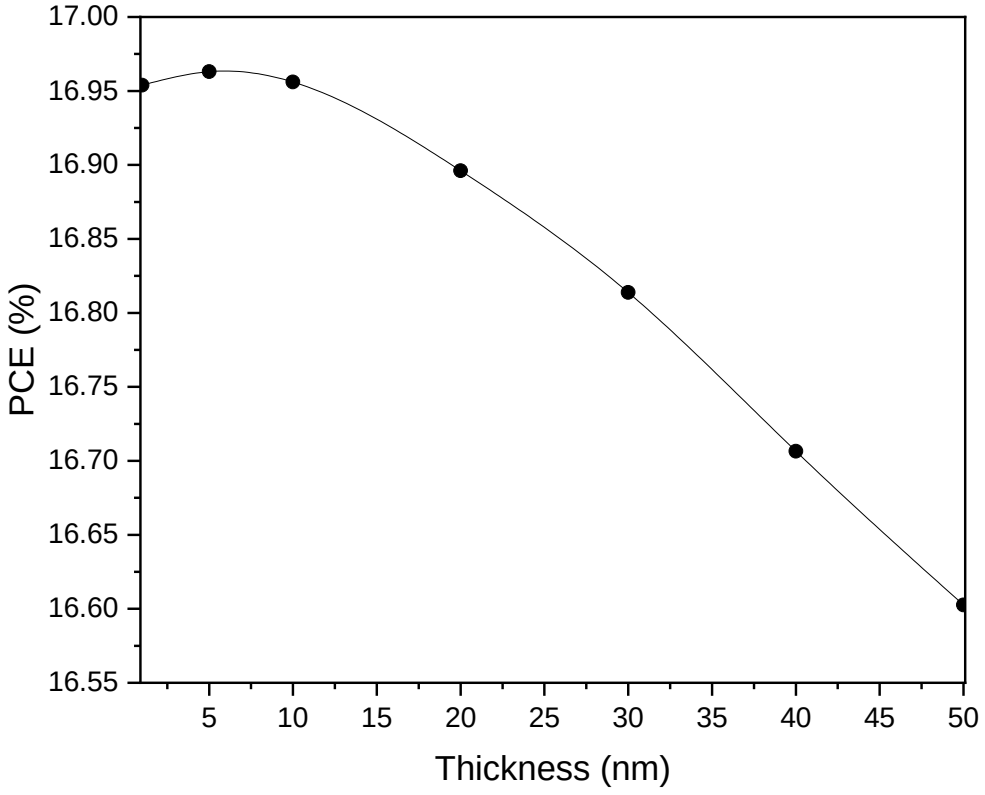

Figure 22: Power conversion efficiency as a function of the thickness of the P3HT hole transport layer.

With the optimal thickness of 0.7 μm the peak efficiency of the solar cell was found to be 15.21 %, as seen in Figure 17. The highest efficiency of 16.96 % is obtained for a P3HT thickness of 5 nm. The differences in efficiency are small, however. With a ten times thicker hole transport layer of 50 nm, the efficiency only decreases to 16.60 %. The obvious result is that the P3HT hole transport layer is a very suitable hole transport material, based on the increase in efficiency. This result shows an increased efficiency with the P3HT hole transport layer, which was also achieved when doing the same experimentally. The experimental results showed an improved current from the solar cell with the thinnest P3HT layer while the thicker layer had very little effect.

Table 8 gives the short circuit current density, open circuit voltage, maximum power, current density and voltage at maximum power point, fill factor and power conversion efficiency. The results show how the HTL improved the efficiency mainly through an increased voltage, observed both at open circuit and maximum power point. The improvements in current density are only minor. This is the exact opposite of what was the case in the experimental part, where a large improvement in current density was observed while the voltage stayed mostly the same. Figure 23 shows how the voltage is improved with the hole transport layer compared to the reference.

Table 8: Results from the modelling for samples with and without HTL. The HTL is a 20 nm thick P3HT layer.

Sample	**J_{SC} (mA)**	**V_{OC} (mV)**	**P_{max} (mW)**	**J_{mpp} (mA)**	**V_{mpp} (mV)**	**FF (%)**	**PCE (%)**
Reference	37.20	536.23	15.21	33.80	450.00	76.27	15.21
P3HT	37.56	618.32	16.90	33.81	500.00	72.78	16.90

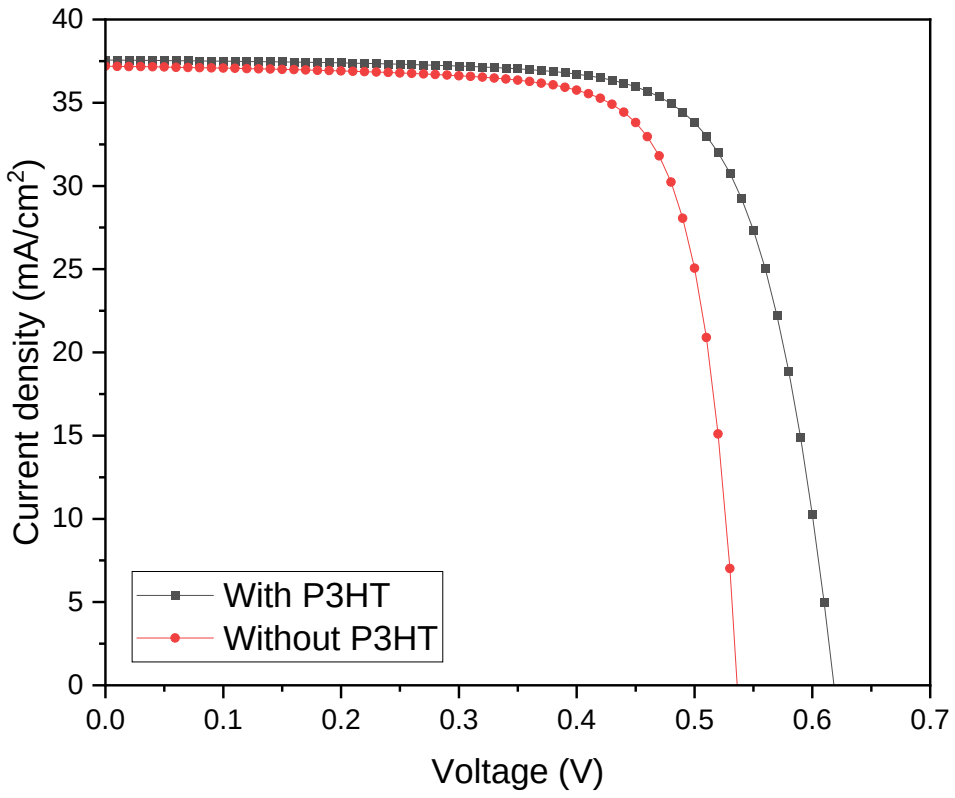

Figure 23: J-V curves for the modelled monofacial solar cells with and without P3HT hole transport layer.

4.7.3 Modelling of bifacial solar cell

As discussed in section 2.4, the performance of the back contact depends on the relation between the work function of the semiconductor and the back contact. Table 9 and Table 10 gives the efficiencies of the samples measured from both the front side and back side, for both monofacial and bifacial samples. The monofacial samples are included for reference. Table 9 gives the results for the samples with hole transport layer, while Table 10 gives the results for the samples with hole transport layer. The ITO work function is varied to analyse if the junction is rectifying or not.

First the results without HTL is considered. As expected, the monofacial cells have a high efficiency from the front side but a very low efficiency from the backside, due to the non-transparent gold back contact. Few photons are able to transmit through the gold contact, so few carriers are generated. Replacing the gold back contact with ITO makes the solar cell bifacial. With the 4.6 eV work function the efficiency is greatly improved for the back side, but still showing below 1 % efficiency. The performance with an ohmic contact is greatly improved, indicating that ITO and absorber forms a rectifying contact. With the ITO work function as ohmic, at 5 eV and 6 eV the efficiency increases for each of them. With these higher work functions for ITO the metal semiconductor becomes non-rectifying, leading to greatly improved efficiencies.

Table 9: Results from modelling of bifacial solar cells without P3HT hole transport layer.

	Back contact work function	**Illumination side**	**PCE**
Monofacial	5.1 eV (Gold)	Back	0.0092 %
		Front	15.21 %
Bifacial	4.6 eV (ITO)	Back	0.41 %
		Front	1.01 %
	Ohmic	Back	4.47 %
		Front	7.97 %
	5 eV	Back	6.57 %
		Front	11.18 %
	6 eV	Back	12.79 %
		Front	13.94 %

For the samples with P3HT the results are largely similar. However, already for the monofacial cells and with the unchanged ITO we see the effect of the P3HT hole transport layer. Comparing to the results without P3HT the efficiencies are improved for both the backside and the front side. The improved performance of the bifacial cell with the HTL indicates that it improves the junction, making it less rectifying. Already for an ohmic contact we see very promising results. With the 5 eV work function for ITO the efficiency is lower than for the ohmic case, indicating that we have a rectifying where the ITO work function is higher than the P3HT work function. This is why the efficiency is lower compared to the ohmic contact, where the work function for the metal is equal to the semiconductor work function. With 6 eV the metal work function surpasses the semiconductor work function, and we see a small improvement in efficiency over the ohmic contact.

Table 10: Results from modelling of bifacial solar cells with P3HT hole transport layer.

	Back contact work function	**Illumination side**	**PCE**
Monofacial	5.1 eV (Gold)	Back	0.012 %
		Front	16.90 %
Bifacial	4.6 eV (ITO)	Back	1.35 %
		Front	2.27 %
	Ohmic	Back	12.89 %
		Front	14.62 %
	5 eV	Back	10.75 %
		Front	12.64 %
	6 eV	Back	13.01 %
		Front	14.75 %

These results shows that bifacial antimony selenide based solar cells can achieve high efficiencies for both the front and back side, if a high enough work function for the back contact is obtained. In addition the P3HT hole transport layer is proven to be suitable also for bifacial applications, showing efficiencies improved over the sample without the hole transport layer.

5 Conclusion and outlook

The thesis investigated antimony selenide based solar cells through fabrication, characterisation and modelling. The aim of the thesis was to work towards the development of high efficiency bifacial thin film solar cells based on antimony selenide. To summarise the work in this thesis the research questions presented in the introduction will be taken up again.

The first research question asked if a P3HT hole transport layer can be used to improve the efficiency of the antimony selenide based solar cell. Solar cells with and without a P3HT hole transport layer was fabricated and characterised. Two thicknesses of the P3HT layer were applied. The characterisation showed that the ticker layer did not improve on the efficiency of the solar cell. With the thinner layer however the efficiency was improved from 4.81 % for the sample without a hole transport layer to 5.34 % for the sample with the hole transport layer. The improvement proved to be caused by a higher current from the solar cell. The use of the hole transport layer was also analysed through modelling. Again, an efficiency increase was obtained when implementing the hole transport layer. However, this time it was mainly caused by an increased voltage, while the current density remained mostly unchanged. Further work is needed to understand the cause of this disagreement. Further research into the effect of the thickness of the P3HT hole transport for the physical devices could be a potential step to further improve the efficiency.

The second research question asked about the effect of using a transparent back contact (ITO) on the performance of the antimony selenide based solar cell under front and rear side illumination. The goal of this question was to investigate if the antimony selenide based solar cells could be made bifacial by replacing the standard gold back contact with the transparent conductive oxide ITO. The samples was prepared both with and without a thin layer of gold between the antimony selenide absorber and the ITO back contact. The thin layer of gold proved to be beneficial for the efficiency of the device, obtained the best efficiency for the bifacial cells of 1.31% under front side illumination and 0.56% under back side illumination. The efficiencies of the bifacial device turned out to be low. The bifacial cells were also researched through modelling. Simulations were performed both with and without the P3HT hole transport layer, and the effect of the work function of the ITO was analysed. The standard bifacial sample modelled showed a decent agreement with the experimental results. Efficiencies of 1.01 % and

0.41 % was obtained from the front and back side respectively. By incorporating both the hole transport and a higher ITO work function, the efficiencies was shown to improve 14.75 % for the front side and 13.01 % for the back side. The use of a higher work function for ITO to obtain a non-rectifying back contact proved to be the needed step to improve the bifacial performance. This indicates that a rectifying junction was formed when applying ITO back contact experimentally, impeding the flow of holes to the back contact. This also illustrates how more work is needed on the ITO back contact. It is suggested to investigate the opportunity to experimentally change the work function of ITO. Research into other suitable back contacts for bifacial applications, with higher work function than ITO, is also a possible approach to further develop the antimony selenide based bifacial solar cell. The P3HT hole transport layer was also shown to improve the performance of the bifacial cells. Experimental implementation of this to investigate the accuracy of the modelling. Due to the small band gap of the P3HT another possible step to improve the back side performance of the bifacial cells could be to investigate the application of hole transport layers with larger band gaps to allow more light to be transmitted to the absorber.

The final research question asked what thickness and doping level of the antimony selenide absorber would results in the best performance of the antimony selenide based solar cell solar cell. This question was researched through modelling. By simulating the antimony selenide based solar cells for varying thicknesses of the absorber layer, a peak efficiency of 15.21 % was achieved for an absorber thickness of 0.7 μm. For thicker absorbers the efficiency was reduced due to recombination, while a thinner absorber exhibited lower efficiencies due to a lacking absorption of light. With the optimal thickness of the absorber the effect of doping the absorber was analysed. However, very small improvements in efficiency was achieved by introducing doping over the intrinsic charge carrier density of antimony selenide. It was found that with an absorber thicker than 0.7 μm, and with a doping density of 10^{16} cm^{-3} the efficiency improved. With a thickness of 4 μm a peak efficiency of 17.36 % was achieved. This is however a thickness of the absorber much higher than the carrier diffusion length of the absorber, and recombination was expected to be too high for this thickness. More work is needed to understand this result. Anyhow increased efficiencies was obtained by increasing the free charge carrier density of the absorber. Therefore, research on the possibilities of experimental doping of antimony selenide to achieve a higher concentration of holes is suggested.

Overall, the work in this thesis have shown that antimony selenide has potential also for applications in bifacial solar cells. Though many challenges remain in order the experimentally achieve the power conversion efficiencies illustrated by the modelling.

6 References

Almora, O., Cabrera, C. I., Garcia-Cerrillo, J., Kirchartz, T., Rau, U., & Brabec, C. J. (2021). Quantifying the Absorption Onset in the Quantum Efficiency of Emerging Photovoltaic Devices. *Advanced energy materials*, *11*(16), 2100022-n/a. https://doi.org/10.1002/aenm.202100022

Baig, F., Khattak, Y. H., Beg, S., & Soucase, B. M. (2019). Numerical analysis of a novel CNT/Cu2O/Sb2Se3/In2S3/ITO antimony selenide solar cell. *Optik (Stuttgart)*, *197*, 163107. https://doi.org/10.1016/j.ijleo.2019.163107

Carron, R., Andres, C., Avancini, E., Feurer, T., Nishiwaki, S., Pisoni, S., Fu, F., Lingg, M., Romanyuk, Y. E., Buecheler, S., & Tiwari, A. N. (2019). Bandgap of thin film solar cell absorbers: A comparison of various determination methods. *Thin Solid Films*, *669*, 482-486. https://doi.org/10.1016/j.tsf.2018.11.017

Černošková, E., Todorov, R., Černošek, Z., Holubová, J., & Beneš, L. (2014). Thermal properties and the structure of amorphous Sb2Se3 thin film. *Journal of thermal analysis and calorimetry*, *118*(1), 105-110. https://doi.org/10.1007/s10973-014-4000-3

Chen, C., Bobela, D. C., Yang, Y., Lu, S., Zeng, K., Ge, C., Yang, B., Gao, L., Zhao, Y., Beard, M. C., & Tang, J. (2017). Characterization of basic physical properties of Sb2Se3 and its relevance for photovoltaics. *Frontiers of Optoelectronics*, *10*(1), 18-30. https://doi.org/10.1007/s12200-017-0702-z

Chen, C., Li, W., Zhou, Y., Chen, C., Luo, M., Liu, X., Zeng, K., Yang, B., Zhang, C., Han, J., & Tang, J. (2015). Optical properties of amorphous and polycrystalline Sb2Se3 thin films prepared by thermal evaporation. *Applied Physics Letters*, *107*(4), 43905. https://doi.org/10.1063/1.4927741

Dadhich, S., Dwivedi, A. D. D., & Singh, A. K. (2021). Fabrication, characterization, numerical simulation and compact modeling of P3HT based organic thin film transistors. *J. Semicond*, *42*(7), 74102. https://doi.org/10.1088/1674-4926/42/7/074102

DNV. (2021). *Energy Transition Outlook 2021*. DNV. https://eto.dnv.com/2021/about-energy-transition-outlook

Green, M. A., Dunlop, E. D., Hohl-Ebinger, J., Yoshita, M., Kopidakis, N., & Hao, X. (2022). Solar cell efficiency tables (version 59). *Progress in photovoltaics*, *30*(1), 3-12. https://doi.org/10.1002/pip.3506

Hofmann, P. (2015). *Solid state physics : an introduction* (2nd. ed.). Wiley.

Honsberg, C. B., & Bowden, S. G. (2019). *Photovoltaics Education Website*. PV Education. https://www.pveducation.org/

Hrostea, L., Leontie, L., Dobromir, M., Doroftei, C., & Girtan, M. (2020). On the Electrical and Optical Properties Stability of P3HT Thin Films Sensitized with Nitromethane Ferric Chloride Solutions. *Coatings (Basel)*, *10*(11), 1. https://doi.org/10.3390/coatings10111074

Huang, L., Wei, Z. L., Zhang, F. M., & Wu, X. S. (2015). Electronic and optical properties of CdS films deposited by evaporation. *Journal of alloys and compounds*, *648*, 591-594. https://doi.org/10.1016/j.jallcom.2015.07.041

Hutter, O. S., Phillips, L. J., Durose, K., & Major, J. D. (2018). 6.6% efficient antimony selenide solar cells using grain structure control and an organic contact layer. *Solar energy materials and solar cells*, *188*, 177-181. https://doi.org/10.1016/j.solmat.2018.09.004

IEA-PVPS. (2021). *Trends in Photovoltaic Applications 2021* (Report IEA PVPS T1-41: 2021). IEA-PVPS. https://iea-pvps.org/trends_reports/trends-in-pv-applications-2021/

IEA. (2021, 6.8). *World gross electricity production by source, 2019*. International Energy Agency,. Retrieved 12.5 from https://www.iea.org/data-and-statistics/charts/world-gross-electricity-production-by-source-2019

Kose, S., Atay, F., Bilgin, V., Akyuz, I., & Ketenci, E. (2010). Optical characterization and determination of carrier density of ultrasonically sprayed CdS:Cu films. *Applied surface science*, *256*(13), 4299-4303. https://doi.org/10.1016/j.apsusc.2010.02.018

Krautmann, R., Spalatu, N., Gunder, R., Abou-Ras, D., Unold, T., Schorr, S., Krunks, M., & Oja Acik, I. (2021). Analysis of grain orientation and defects in Sb2Se3 solar cells fabricated by close-spaced sublimation. *Solar Energy*, *225*, 494-500. https://doi.org/10.1016/j.solener.2021.07.022

Li, D.-B., Yin, X., Grice, C. R., Guan, L., Song, Z., Wang, C., Chen, C., Li, K., Cimaroli, A. J., Awni, R. A., Zhao, D., Song, H., Tang, W., Yan, Y., & Tang, J. (2018). Stable and efficient CdS/Sb2Se3 solar cells prepared by scalable close space sublimation. *Nano energy*, *49*(C), 346-353. https://doi.org/10.1016/j.nanoen.2018.04.044

Li, S., Cao, Y.-L., Li, W.-H., & Bo, Z.-S. (2021). A brief review of hole transporting materials commonly used in perovskite solar cells. *Rare metals*, *40*(10), 2712-2729. https://doi.org/10.1007/s12598-020-01691-z

Li, Z., Liang, X., Li, G., Liu, H., Zhang, H., Guo, J., Chen, J., Shen, K., San, X., Yu, W., Schropp, R. E. I., & Mai, Y. (2019). 9.2%-efficient core-shell structured antimony selenide nanorod array solar cells. *Nat Commun*, *10*(1), 125-125. https://doi.org/10.1038/s41467-018-07903-6

Lin, L.-y., Jiang, L.-q., Qiu, Y., & Fan, B.-d. (2018). Analysis of Sb2Se3/CdS based photovoltaic cell: A numerical simulation approach. *The Journal of physics and chemistry of solids*, *122*, 19-24. https://doi.org/10.1016/j.jpcs.2018.05.045

Liu, F., Lai, Y., Liu, J., Wang, B., Kuang, S., Zhang, Z., Li, J., & Liu, Y. (2010). Characterization of chemical bath deposited CdS thin films at different deposition temperature. *Journal of alloys and compounds*, *493*(1), 305-308. https://doi.org/10.1016/j.jallcom.2009.12.088

Liu, T., Chen, K., Hu, Q., Zhu, R., & Gong, Q. (2016). Inverted Perovskite Solar Cells: Progresses and Perspectives. *Adv. Energy Mater*, *6*(17), 1600457-n/a. https://doi.org/10.1002/aenm.201600457

Mamta, Maurya, K. K., & Singh, V. N. (2022). Influence of buffer layers on antimony selenide based solar cell. *Optical materials*, *126*. https://doi.org/10.1016/j.optmat.2022.112240

Mavlonov, A., Razykov, T., Raziq, F., Gan, J., Chantana, J., Kawano, Y., Nishimura, T., Wei, H., Zakutayev, A., Minemoto, T., Zu, X., Li, S., & Qiao, L. (2020). A review of Sb2Se3 photovoltaic absorber materials and thin-film solar cells. *Solar Energy*, *201*, 227-246. https://doi.org/10.1016/j.solener.2020.03.009

MIT. (2015). *The Future of Solar Energy*. MIT. https://energy.mit.edu/research/future-solar-energy/

NREL. (n.d.). *Reference Air Mass 1.5 Spectra*. https://www.nrel.gov/grid/solar-resource/spectra-am1.5.html

Pearsall, N. M. (2017). Introduction to photovoltaic system performance. In (pp. 1-19). https://doi.org/10.1016/B978-1-78242-336-2.00001-X

Philipps, S., & Warmuth, W. (2022). *Photovoltaics Report*. F. ISE. https://www.ise.fraunhofer.de/en/publications/studies/photovoltaics-report.html

Pokhrel, D., Bastola, E., Khanal Subedi, K., Rijal, S., Jamarkattel, M. K., Awni, R. A., Phillips, A. B., Yan, Y., Heben, M. J., & Ellingson, R. J. (2022). Copper iodide nanoparticles as a hole transport layer to CdTe photovoltaics: 5.5 % efficient back-illuminated bifacial CdTe solar cells. *Solar energy materials and solar cells*, *235*, 111451. https://doi.org/10.1016/j.solmat.2021.111451

Schneider, T., Dethloff, C., Hölscher, T., Kempa, H., & Scheer, R. (2022). Comparison of Mo and ITO back contacts in CIGSe solar cells: Vanishing of the main capacitance step. *Progress in photovoltaics*, *30*(2), 191-202. https://doi.org/10.1002/pip.3476

Silvaco, I. (2019). *Atlas User Manual*.

Spalatu, N., Krautmann, R., Katerski, A., Karber, E., Josepson, R., Hiie, J., Acik, I. O., & Krunks, M. (2021). Screening and optimization of processing temperature for Sb2Se3 thin film growth protocol: Interrelation between grain structure, interface intermixing and solar cell performance. *Solar energy materials and solar cells*, *225*, 111045. https://doi.org/10.1016/j.solmat.2021.111045

Streetman, B. G., & Banerjee, S. (2016). *Solid state electronic devices* (7th , global ed.). Pearson.

VDMA. (2022). *International Technology Roadmap for Photovoltaic*. VDMA. https://www.vdma.org/international-technology-roadmap-photovoltaic